1 Design of novel Cyanovirin-N variants by modulation of binding dynamics through distal 2 mutations 3 I. Can Kazan^{1,2}¶, Prerna Sharma¹¶, Mohammad Imtiazur Rahman¹¶, Andrey Bobkov³, Raimund 4 Fromme¹, Giovanna Ghirlanda^{1*}, S. Banu Ozkan²* 5 6 7 ¹School of Molecular Sciences, Arizona State University, Tempe, AZ 8 ²Center for Biological Physics and Department of Physics, Arizona State University, Tempe, AZ 9 ³Sanford Burnham Prebys Medical Discovery Institute, La Jolla, CA 10 11 *Corresponding authors 12 Email: Giovanna.Ghirlanda@asu.edu 13 Banu.Ozkan@asu.edu 14 15 These authors contributed equally to this work. 16 17 **Abstract** 18 19 We develop integrated coevolution and dynamic coupling (ICDC) approach to identify, 20 mutate, and assess distal sites to modulate function. We validate the approach first by analyzing 21 the existing mutational fitness data of TEM-1 β-lactamase and show that allosteric positions co-22 evolved and dynamically coupled with the active site significantly modulate function. We further 23 apply ICDC approach to identify positions and their mutations that can modulate binding affinity

in a lectin, Cyanovirin-N (CV-N), that selectively binds to dimannose, and predict binding energies of its variants through Adaptive BP-Dock. Computational and experimental analyses reveal that binding enhancing mutants identified by ICDC impact the dynamics of the binding pocket, and show that rigidification of the binding residues compensates for the entropic cost of binding. This work suggests a general mechanism by which distal mutations modulate function through dynamic allostery and provides a blueprint to identify candidates for mutagenesis in order to optimize protein function.

Introduction

The evolutionary history of a protein comprises the ensemble of mutations acquired during the course of its evolutionary trajectory across different species, and contains valuable information on which residue positions contribute the most to a given protein's 3-D fold and function based on their conservation. (Campbell et al., 2016; Rivoire et al., 2016; Yang et al., 2016). Furthermore, the subset of positions that are co-evolved (i.e., correlated mutational sites) provide clues on specific, native-state interactions. Pairwise residue contacts inferred from co-evolved positions within a protein family can be used as distance restraints to accurately model 3-D structures. (de Juan et al., 2013; Hopf et al., 2019; Kamisetty et al., 2013; Kim et al., 2014; Tripathi et al., 2015). Recent revolutionary successes in accurate predictions of 3-D protein structures combine these methods with machine learning strategies i.e., deep learning (Jumper et al., 2021; Wang et al., 2016; Xu, 2019). Co-evolved positions also embed information on protein function, for example revealing how factors such as binding affinity and specificity are modulated across evolutionary history and species (Rivoire et al., 2016; Salinas and Ranganathan, 2018; Torgeson et al., 2022).

However, accessing, interpreting, and applying this information in a predictive manner is very challenging; mutations observed in the evolutionary history are often distal from the functional sites, implying that protein dynamics are responsible for their effects on function and that these sites act as distal allosteric regulators of function (Campitelli et al., 2020a; Modi et al., 2021a; Romero and Arnold, 2009; Salinas and Ranganathan, 2018; Tokuriki et al., 2012; Torgeson et al., 2022; Wei et al., 2016).

53

54

55

56

57

58

59

60

61

62

63

64

65

66

67

68

69

47

48

49

50

51

52

Molecular dynamics (MD) simulations can capture protein dynamics and reveal the impact of distal mutations on function (Bowman and Geissler, 2012; Campbell et al., 2016; Campitelli et al., 2020a; Jiménez-Osés et al., 2014; Kolbaba-Kartchner et al., 2021; Modi et al., 2021a; Yang et al., 2016). However, the computational cost of MD simulations of sufficient length can be prohibitively high; further, it's often far from straightforward to forge a clear connection to function. To bridge this gap, we developed a framework to quickly evaluate MD trajectories and identify the sensitivity of a given position to mutation based on its intrinsic flexibility, which we assess using our Dynamic Flexibility Index (DFI) metric, and on its dynamic coupling with functionally critical positions assessed by Dynamic Coupling Index (DCI) (Campitelli et al., 2018; Gerek and Ozkan, 2011; Kumar et al., 2015b; Larrimore et al., 2017). DFI measures the resilience of a position by computing the total fluctuation response and thus captures the flexibility/rigidity of a given position. Applying DFI to several systems, we showed that rigid positions such as hinge sites contribute the most to equilibrium dynamics, and that mutations at hinge sites significantly impact function regardless of the distance from active sites (Kim et al., 2015; Kolbaba-Kartchner et al., 2021; Modi et al., 2021b, 2018; Modi and Ozkan, 2018; Zou et al., 2021, 2015). DCI measures the dynamic coupling between residue pairs and thus identifies positions most strongly

coupled to active/binding sites; these positions point to possible allosteric regulation sites important for modulating function in adaptation and evolution (Butler et al., 2015; Campitelli et al., 2020a, 2021; Kuriyan and Eisenberg, 2007; Lu and Liang, 2009; Modi and Ozkan, 2018; Ose et al., 2020; Risso et al., 2018; Wodak et al., 2019).

In this paper, we present integrated co-evolution and dynamic coupling (ICDC) approach to identify distal allosteric sites, and to assess and predict the effects of mutations on these sites on function. We propose a system to classify residue positions in a binary fashion based on co-evolution (co-evolved, 1 or not, 0) and dynamic coupling by DFI and DCI (dynamically coupled 1, or not, 0) with the functionally critical sites. This classification captures the complementarity of dynamics-based and sequence-based methods. We hypothesize that positions belonging to category (1,1), i.e., positions both co-evolved and dynamically coupled with the functional sites, will have the largest effect on function.

We validate our hypothesis first by analyzing the existing mutational fitness data for TEM-1 β-lactamase, available for every position of the protein (Stiffler et al., 2015). In agreement with our hypothesis, we find that mutations on category (1,1) positions significantly modulate the function. A large fraction of mutations enhancing enzymatic activity correspond to category (1,1) irrespective of distance from the active site. Second, we apply our ICDC approach to blindly predict and experimentally validate mutations that allosterically modulate dimannose binding in a natural lectin, Cyanovirin-N (CV-N). CV-N binds dimannose with nanomolar affinity and remarkable specificity (Barrientos et al., 2003; Botos and Wlodawer, 2005, 2003; Mori and Boyd, 2001; O'Keefe et al., 2003). It is part of the CV-N family, found in a wide range of organisms

including cyanobacterium, ascomycetous fungi, and fern (Koharudin et al., 2008; Koharudin and Gronenborn, 2013; Patsalo et al., 2011; Percudani et al., 2005; Qi et al., 2009). While the 3D folds is remarkably conserved in all experimentally characterized members, the affinity and specificity for different glycans and, in particular, to dimannose varies significantly (Koharudin et al., 2009, 2008; Matei et al., 2016; Woodrum et al., 2013). To design CV-N variants with improved binding affinities for dimannose based on distal allosteric coupling, we binned each position in one of the four categories based on computed DFI, DCI and co-evolution rates. We explored mutations at these sites based on frequency in the sequence alignment. After obtaining the mutant models through Molecular dynamics (MD) simulations, we assessed the impact of each naturally observed mutation on binding affinity by docking dimannose to the mutant models via Adaptive BP-Dock (Bolia et al., 2014b, 2014a; Bolia and Ozkan, 2016). We chose position I34, which belongs to category (1,1) and is 16Å away from the binding pocket, for experimental validation. We found that mutations I34K/L/Y had a diverse effect on glycan binding, either improving by two-fold or abolishing completely. Through experimental and MD studies we show that the observed improvement in binding affinity is due to changes in the dynamics of residues in the binding pocket; mutation I34Y leads to rigidification of binding sites, thus compensating the entropic cost of binding (Breiten et al., 2013; Chodera and Mobley, 2013; Cornish-Bowden, 2002; Fox et al., 2018). Mutations at an additional position (A71T/S) from category (1,1) showed evidence of the same allosteric mechanism governing the modulation of binding dynamics. Overall, this study provides not only a new approach to identify distal sites whose mutations modulate binding affinity, but also sheds light into mechanistic insights on how distal mutations modulate binding affinity through dynamics allostery.

93

94

95

96

97

98

99

100

101

102

103

104

105

106

107

108

109

110

111

112

113

Results and Discussion

Combining long-range dynamic coupling analysis with co-evolution allows to identify distal sites that contribute to functional activity.

With our ICDC approach, we aim to explore the role of dynamics versus evolutionary coupling as well as the role of rigidity versus flexibility in allosterically modulating active/binding site dynamics. To this extend, we created four unique categories that classifies residue positions based on residue DFI score, DCI score and co-evolutionary score: category (1,1) is dynamically, and co-evolutionarily coupled rigid sites (exhibiting %DFI values 0.2 or lower, showing 0.7 or higher %DCI with the binding site, and showing 0.6 or higher co-evolution scores with the binding site); category (1,0) is dynamically coupled but co-evolutionarily not coupled sites; category (0,1) is dynamically not coupled but co-evolutionarily coupled sites; category (0,0) is dynamically not coupled, and co-evolutionarily not coupled flexible sites (exhibiting %DFI values 0.7 or higher) (Supplementary file 1 table 1 & 2); importantly, this classification is based on two independent statistical approaches thus compensate the noise of individual approaches. Based on our evolutionary analysis (Campitelli et al., 2020a; Modi et al., 2021b; Modi and Ozkan, 2018), we hypothesize that category (1,1) would impact protein activity or binding affinity the most.

To test our hypothesis, we first analyzed the deep mutational scanning data available for the beta lactamase TEM-1, correlating changes in ampicillin degradation activity (e.g. MIC values) with mutations to all possible amino acids at each position (Stiffler et al., 2015). The experimental results showed that amino acid substitutions at the catalytic site residues of TEM-1 negatively

impacted activity. Mutations at other positions also affected activity; while most mutations were deleterious, surprisingly, others resulted in increased activity. The impact of mutations on dynamics and function of TEM-1 have been heavily explored but the distal mutational effects are still poorly understood (Kolbaba-Kartchner et al., 2021; Modi et al., 2021b; Modi and Ozkan, 2018; Salverda et al., 2010; Schneider et al., 2021; Stiffler et al., 2015; Thomas et al., 2010; Zimmerman et al., 2017; Zou et al., 2015). We applied our approach by obtaining DFI, DCI and co-evolution scores for every position of TEM-1 and binning residue positions into each ICDC category (Table S1). We constructed fitness distributions for each category using the experimentally measured single mutant relative fitness values for all mutations per position provided in the dataset (Fig 1).

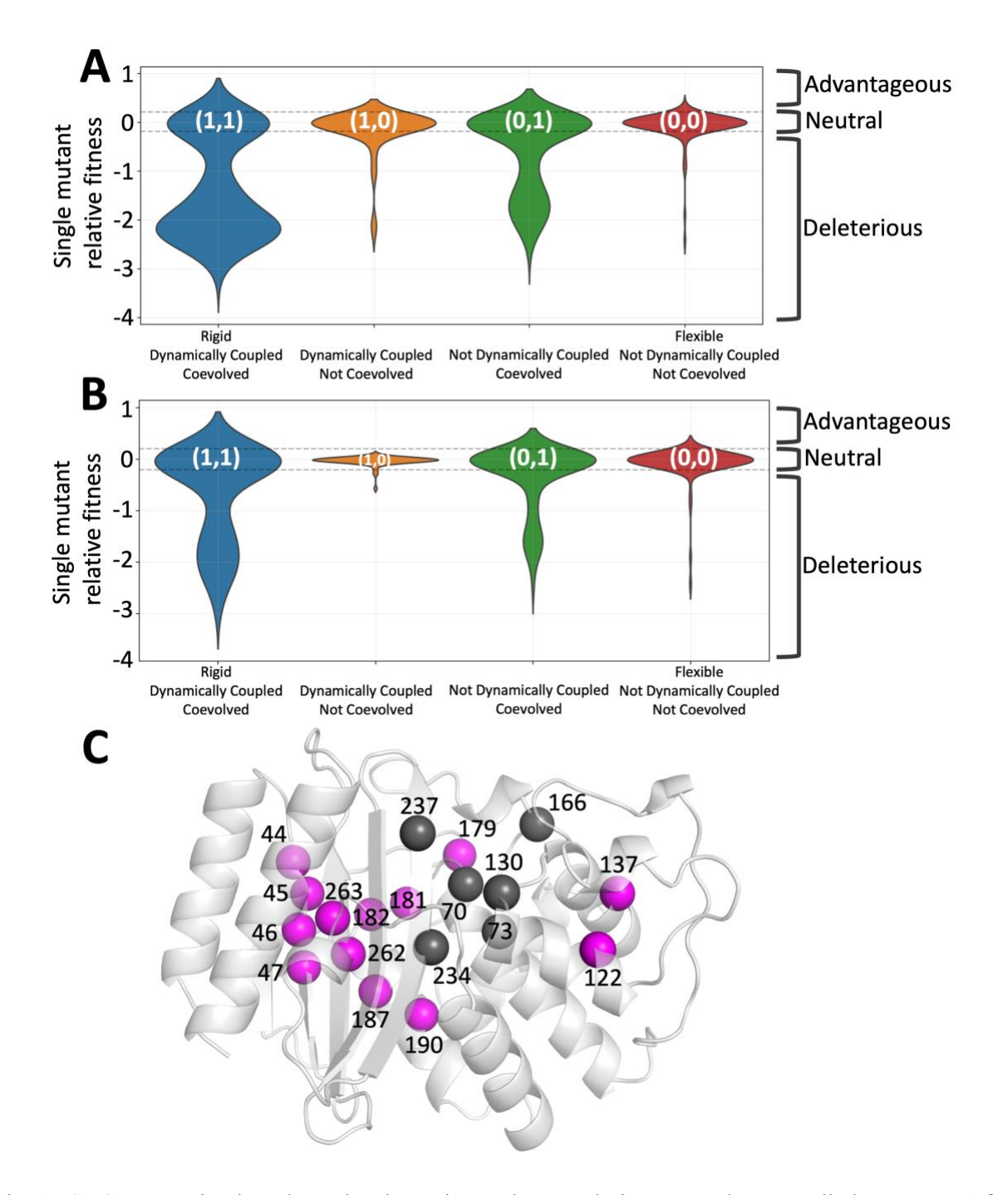


Fig 1 ICDC categories based on the dynamics and co-evolutionary analyses applied on TEM-1 β-lactamase. A) The distributions in the form of violin plots are obtained for each ICDC category using all available experimental mutational data (Stiffler et al., 2015) B) Violin plots showing the fitness values for amino acid substitutions observed in the natural sequences. C) The category (1,1) positions are mapped on 3-D structure. The catalytic site residues are shown in dark grey whereas category (1,1)

positions are shown in magenta color. The function altering category (1,1) positions are widely distributed over the 3-D structure.

We found that category (1,1) positions show the highest impact, both significantly enhancing and reducing ampicillin degradation by TEM-1 (Fig 1A&C). In addition, category (0,0) residue mutations (i.e., the exact opposite of category (1,1)) lie within the neutral like activity range defined by Stiffler et al., 2015, suggesting that mutations on positions that neither co-evolve nor dynamically couple to active site do not affect the function significantly. Category (1,0) residues enhance activity more than those in the neutral category (0,0). Mutations in category (0,1) positions also modulate function in both positive and negative direction, albeit not as strongly as those in category (1,1). However, mutations that negatively impact activity are conspicuously under-represented in the MSA of native sequences (Fig 1B), particularly in category (1,1). This finding implies nature mostly allows mutations that don't compromise fold and function: Negative selection (i.e. elimination of amino-acid types that are detrimental to the folding) is a major force in shaping the mutational landscape (Jana et al., 2014; Modi et al., 2021a; Morcos, 2020; Morcos et al., 2014, 2013). Thus, the use of conservation information from MSA is a useful tool in eliminating deleterious amino acid substitutions in protein design.

Our ICDC selection criteria effectively identifies residue positions and their amino acid substitutions that could finetune function without leading to a functional loss; and category (1,1) residues have the largest impact on function irrespective of their distance from active site (Fig 1C).

Application of ICDC approach to modulate CV-N binding affinity through distal mutations

CV-N is a small (11 kDa) natural lectin isolated from cyanobacterium *Nostoc ellipsosporum* which comprises two quasi-symmetric domains, A (residues 1-38/90-101) and B (residues 39-89 respectively), that are connected to each other by a short helical linker. Despite almost having identical structures, the domains show relatively low sequence homology (28% sequence identity, and 52% similarity). Functionally, they both bind dimannose, yet the affinity is quite different, with domain B having tighter binding affinity (K_d = 15.3 μ M), and domain A showing weak affinity (K_d = 400 μ M) (Balzarini, 2007; Bolmstedt et al., 2001; Li et al., 2015).

To simplify our analyses, we used a designed CV-N variant, P51G-m4, that contains a single high-affinity dimannose binding site (domain B), folds exclusively as a monomer in physiological conditions, and is more stable to thermal denaturation than wild type (Fromme et al., 2008, 2007). The binding pocket of domain B of CV-N has been subjected to intense scrutiny to glean information on the origin of its binding specificity for dimannose (Bewley, 2001; Bolia et al., 2014b; Botos and Wlodawer, 2003; Li et al., 2015; Vorontsov and Miyashita, 2009). Previous mutational studies on the binding pocket residues have shown their importance in modulating interaction with dimannose (Barrientos et al., 2006; Bolia et al., 2014b; Chang and Bewley, 2002; Matei et al., 2008). All known substitutions of the binding residues led to decreased binding affinity for dimannose on domain B (Bolia et al., 2014b; Fujimoto and Green, 2012; Kelley et al., 2002; Matei et al., 2011; Ramadugu et al., 2014). Evolutionary analyses shows that the majority of the binding site residues are conserved in CV-N glycan interactions, suggesting that affinity is already optimized at the binding site. (Koharudin et al., 2008; Percudani et al., 2005). We

hypothesized that amino acid substitutions at distal positions could enhance the dimannose affinity of CV-N by rigidification of the binding site and applied our ICDC approach to CV-N to identify positions in each category (Table S2) (Supplementary file 1 table 2).

198

199

200

201

202

203

204

205

206

207

208

209

210

211

212

213

214

215

216

217

195

196

197

We generated models of CV-N variants in each ICDC category by mutating these positions to amino acid types observed in the MSA of CV-N family members, choosing the subset of sequences that have binding sites with identical or similar amino-acid composition to P51G-m4 CV-N. As discussed above this approach allows us to identify amino-acid substitutions with the least impact on fold. All the substitutions identified (104 variants in total) were modeled using the crystal structure of P51G-m4 CV-N (Fromme et al., 2008) and subjected to MD simulations (Abraham et al., 2015; Spoel et al., 2005). The best conformation sampled for each variant obtained from equilibrated production trajectories was used as a model for dimannose docking analysis. We evaluated the variants using Adaptive BP-Dock (Bolia and Ozkan, 2016), a computational docking tool that incorporates both ligand and receptor flexibility to accurately sample binding induced conformations, and ranks them using X-scores binding energy units (XEUs). In previous work on CV-N this method yielded good correlations with experimentally measured binding affinities (K_d) , and established -6.0 XEU unit as a good threshold to differentiate variants that bind dimannose from "non-binders" (Bolia et al., 2014b; Li et al., 2015; Woodrum et al., 2013). Here, we applied Adaptive BP-Dock initially on wild-type CV-N and its variants, P51G-m4 and mutDB (a mutant in which binding by domain B has been obliterated) and the results recapitulate the success of previous studies (Table S3). This result shows that Adaptive BP-Dock can correctly assess the dimannose binding of CV-N and its variants, thus, we applied it on new P51G-m4 CV-N variants to predict the impact of mutations on dimannose binding. Figure 2 shows the distribution of changes in predicted binding energy scores relative to the P51G-m4 energy scores for mutations belonging to each binary category: a positive change in binding score represents an unfavorable effect on binding, and, conversely, a negative change in the score indicates an enhancement in binding.



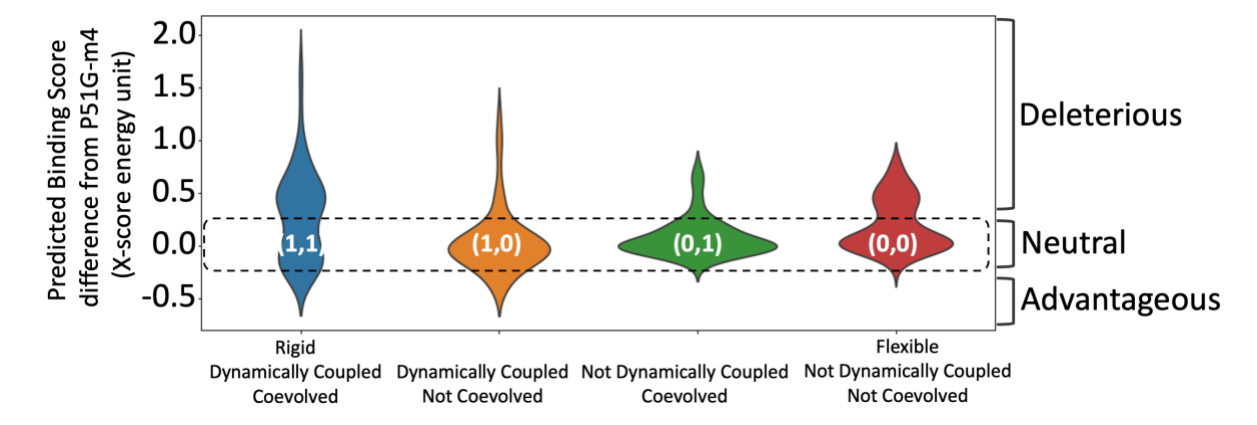


Fig 2 Predicted binding energies for each ICDC category. Mutations in category (1,1) positions comprise the highest number of binding energy enhancing mutations as well as deleterious mutations. Mutations in category (0,0) positions are mostly near neutral (Category (1,1) & (0,0) P value < 0.3).

The substitutions on positions in category (1,1) (Fig 2) yield a wide range of change in binding energy scores: the tail of the distribution on the positive side reaches nearly a binding score change of 2.0 XEUs and on the negative site values below -0.5 XEUs. Strikingly, the positions in category (1,1) yield the most binding enhancing energy scores compared to all other categories, mirroring TEM-1 results. Additionally, the substitutions applied in category (1,0) also result in more favorable binding energy scores for dimannose. Mutations in both category (1,1) and (1,0) present favorable binding energy scores. However, the number of mutations predicted to be enhancing binding in category (1,1) is more than those in category (1,0) (26% of category (1,1) compared to 14% of category (1,0)). Interestingly, the mutations in category (1,0) that disrupt the

binding energy scores is not a strong as category (1,1), but similar to category (0,1) and (0,0). The observed mostly neutral behavior with category (0,0) agrees with the same trend obtained with TEM-1 analyses.

Overall, the distribution of computational binding scores of dimannose binding to CV-N in each category aligns with the distribution of experimentally characterized TEM-1 fitness results of the same category. However, there are some discrepancies, for example, there are beneficial mutations in category (0,1) in TEM-1, but we don't observe the same trend in CV-N. This is due to the initial challenge faced in constructing the MSA of CV-N homologous proteins. There is limited sequence information, and most of the proteins in the CV-N family exhibits binding specificity to a different glycan (Fujimoto and Green, 2012; Koharudin et al., 2009). In contrast, β-lactamase family proteins exhibit highest activity towards penicillin, and they have been subjected to strong natural selection leading to conservation in both fold and function (Salverda et al., 2010; Zou et al., 2021). Hence, the less noise in evolutionary analysis in case of β-lactamase family of proteins allows us to correctly filter deleterious type of substitutions based on the MSA. Regardless, however, in both cases, as hypothesized, substitutions on category (1,1) residues impact the function most.

To further investigate the mechanism of functional modulation of category (1,1) mutations, we chose the position with highest binding enhancing docking scores, I34, from category (1,1). I34 exhibits %DFI values lower than 0.2 (Fig 3A), is at least 16Å away from binding residues (distal), dynamically coupled (Fig 3B) and co-evolved with the binding pocket (Table S2) (Supplementary file 1 table 2). Moreover, docking scores of I34 variants suggest that the mutations

can modulate binding in a wide range: I34Y variant leads to an increase in binding affinity (beneficial), I34K decreases the binding affinity (deleterious), and I34L yields no change (neutral) (Table 1).



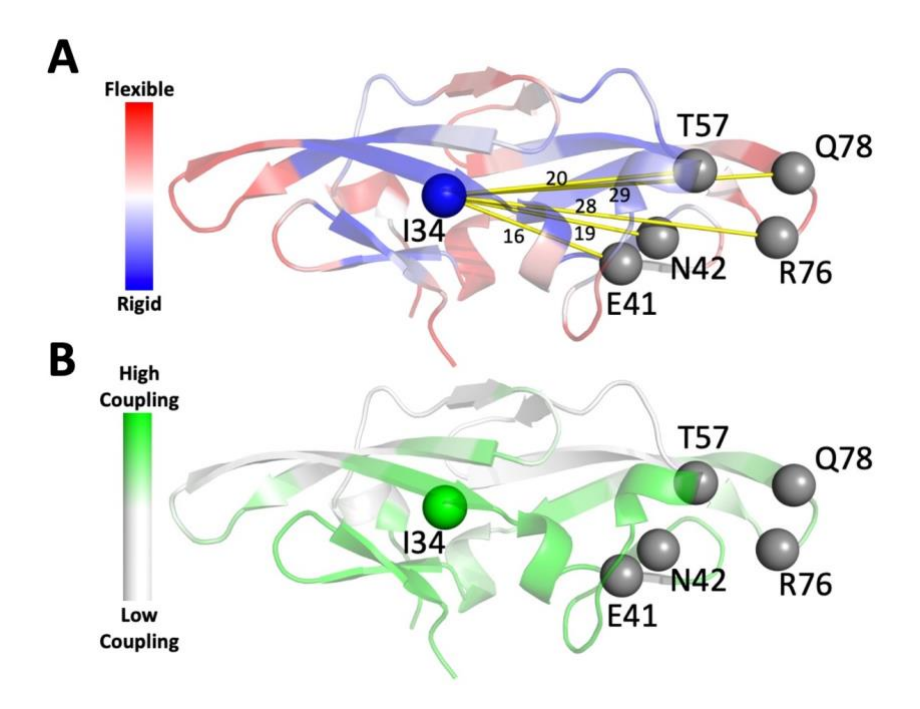


Fig 3 A) DFI profile mapped onto CV-N structure: red corresponds to high DFI, (very flexibile sites), and blue to low DFI values (hinge sites). Position I34 (low DFI score) is highlighted B) DCI profile projected on CV-N structure with green corresponding to sites exhibiting high coupling with binding site residues.

To verify the predictions of I34 variants, we first assessed the folding and thermal stability of these mutants by circular dichroism (CD) spectroscopy. Far-UV CD spectroscopy showed that all mutants are well folded and adopt a fold similar to the parent protein, characterized by spectra with a single negative band centered at 216 nm. We determined the stability of the mutants by CD monitored thermal denaturation; the thermal denaturation curves were analyzed to obtain apparent

melting temperature (T_m) values. We found that the conservative mutation I34L is as stable as P51G-m4, with apparent T_m of 57.8 °C and 58 °C respectively. In contrast, I34Y and I34K were less thermostable than P51G-m4 as shown by apparent T_m values of 54.7 °C and 47 °C, respectively. Not surprisingly, substituting a hydrophobic residue with a basic aliphatic amino acid (lysine) has a large destabilizing effect, while aromatic and polar tyrosine is better tolerated. The trend of thermostability is P51G-m4 ~ I34L > I34Y > I34K (Fig S1).

Table 1. Predicted binding affinities of domain B, experimental ITC data, and chemical denaturation experiments for P51G-m4, and its I34 variants.

Protein	Predicted Binding Score (X-score energy unit)	ITC dimannose K _d (µM)	ITC dimannose ΔH (kcal/mol)	ITC dimannose TAS (kcal/mol) (T=298K)	ITC dimannose ΔG (kcal/mol)	ΔG _{H2O} (kcal/mol)	C _m (M)
P51G-m4	-6.62	117 ± 3	-12.3 ± 0.3	-7.00 ± 0.3	-5.30 ± 0.3	3.01 ± 0.047	1.46 ± 0.019
P51G-m4-I34K	-5.85	No-binding	No-binding	No-binding	No-binding	2.40 ± 0.124	0.68 ± 0.015
P51G-m4-I34L	-6.19	148 ± 2	-9.60 ± 0.1	-4.40 ± 0.1	-5.20 ± 0.1	2.95 ± 0.077	1.39 ± 0.009
P51G-m4-I34Y	-6.75	64 ± 5	-4.35 ± 0.1	1.32 ± 0.2	-5.67 ± 0.2	2.91 ± 0.157	1.13 ± 0.017

Chemical denaturation experiments were used to extract thermodynamic values, after ensuring complete equilibration at each concentration of guanidinium hydrochloride by incubating the samples for 72-hour (Patsalo et al., 2011). The ΔG_{H20} values and C_m values of P51G-m4, I34L, I34Y and I34K are found as 3.0, 2.94, 2.91 and 2.38 kcal/mol and of 1.45, 1.39, 1.13 and 0.68 M respectively (Table 2). The results align with the thermal denaturation results: P51G-m4 is the most stable to denaturant, followed by I34L, I34Y and I34K (Fig S2).

Next, we evaluated the impact of the mutations on the dimannose binding affinity by isothermal titration calorimetry (ITC) (Fig S3); data were analyzed to extract K_d values listed in Table 2. We found that I34Y binds dimannose with tightest affinity (K_d : 64 μ M) of all the mutants tested, a two-fold improvement over P51G-m4 (K_d : 117 μ M). Binding by I34L is slightly weaker with a K_d of 148 μ M. No binding was observed for I34K in these conditions. Thermodynamic values extracted from ITC experiments (Table 2) suggest that entropy changes play an important role in the observed changes in binding affinity: surprisingly, entropy is positive for I34Y, indicating an increase in disorder upon binding.

To glean more information on the mode of binding by I34Y, we determined the X-ray structure of the unbound and dimannose-bound form and compared it with the template protein P51G-m4. The fold is highly conserved (Fig 4) as shown by main chain RMSD of 0.16 and 0.20 Å with bound and unbound I34Y, respectively, and tyrosine is well tolerated at position I34. The binding pocket region is also structurally conserved compared to P51G-m4. Analysis of the polar contacts between dimannose and P51G-m4 and I34Y (Fig 4B) shows an identical number of hydrogen bonds (11) with the ligand, indicating a conserved binding pose. We compared the docked pose of I34Y acquired from Adaptive BP-Dock with the bound X-ray structure. The ligand shows an RMSD value of 0.75 Å (Fig S4). These observations suggest that the increase in binding affinity of I34Y towards dimannose might be mediated by equilibrium dynamics, which are not captured by the crystal structure. This hypothesis is supported by the changes in entropy compensation measured experimentally (ITC) in dimannose binding by P51G-m4 (negative TΔS) and I34Y (positive TΔS).

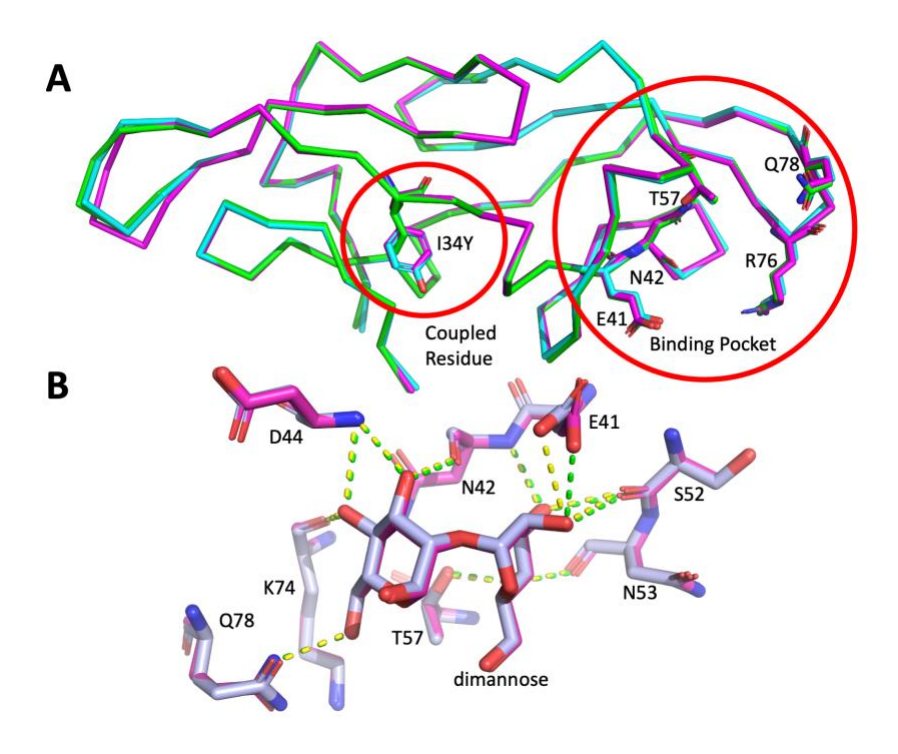


Fig 4 A) The crystal structures of I34Y (bound in magenta and unbound in cyan) and its template protein P51G-m4 (green) are superimposed. B) Overlay of bound structures of I34Y (magenta) and P51G-m4 (grey) (RMSD 0.15 Å); dashed lines depict polar interactions with dimannose.

Molecular mechanism governing the binding dynamics in I34 variants

It is interesting to observe that a distal site can modulate binding affinity to a wide range based on amino-acid substitutions. This finding has also been observed for allosterically regulated enzymes such as LacI, for which different amino-acid substitutions on non-conserved sites lead to gradual changes in function, acting like a rheostatic switch to modulate function through conformational dynamics (Campitelli et al., 2021, 2020b; Meinhardt et al., 2013; Miller et al., 2017; Swint-Kruse et al., 1998). To gather atomic level detail on how the substitutions on I34 dynamically modulate the binding affinity, we employed MD simulations both in bound and unbound forms (See Methods for details of the simulations). The unbound trajectories were

analyzed for acquiring binding pocket hydrogen bond distances and pocket volume. Later, to learn about the ligand induced conformational dynamic changes, the bound trajectories were utilized to estimate computational binding free energies (Deng and Roux, 2009; Okazaki et al., 2006).

Previous computational work in our lab had linked binding affinity in the CV-N family to the accessibility of the binding pocket: A hydrogen bond between the amide hydrogen of N42 and carbonyl oxygen of N53 forms a closed pocket, hindering glycan accessibility, whereas the loss of this hydrogen bond leads to an open pocket (Li et al., 2015). Using the formation of this hydrogen bond in the trajectories of unbound WT and I34Y as metric for assessing open and closed conformations, we found that I34Y variant samples the open binding pocket more often than P51G-m4 (Fig S5).

Another compelling evidence differentiating I34 variants from P51G-m4 is the change in their binding pocket volumes estimated by POVME pocket volume calculation tool (Wagner et al., 2017). The calculated pocket volumes for I34Y, I34K and P51G-m4 were converted into frequencies to obtain probability distributions (Fig 5A), revealing that I34Y variant samples a more compact pocket volume compared to P51G-m4. If the pocket is too small or too large, dimannose cannot maximize its interaction with the protein, and a compact conformation enables dimannose to easily make the necessary hydrogen bond interactions with the protein. This optimum pocket volume sampled by I34Y may also explain the different binding energetics observed by ITC, in which a positive entropy change upon binding compensates for the loss in enthalpy compared to P51G-m4 (Table 1) (Breiten et al., 2013; Cornish-Bowden, 2002). Pocket volume analysis reveals a larger value for I34K compared to P51G-m4, suggesting that this mutant cannot accommodate

the necessary interactions with the dimannose resulting in loss of binding. We applied the same pocket volume calculation to the X-ray structures of P51G-m4 and I34Y variant, and we found volumes of 141 Å³ and 114 Å³ for P51G-m4 and I34Y, respectively in the unbound forms (Fig 5B). These volumes correlate well with the mean volumes from MD trajectories, suggesting that the variants modulate the conformational dynamics of binding pocket.

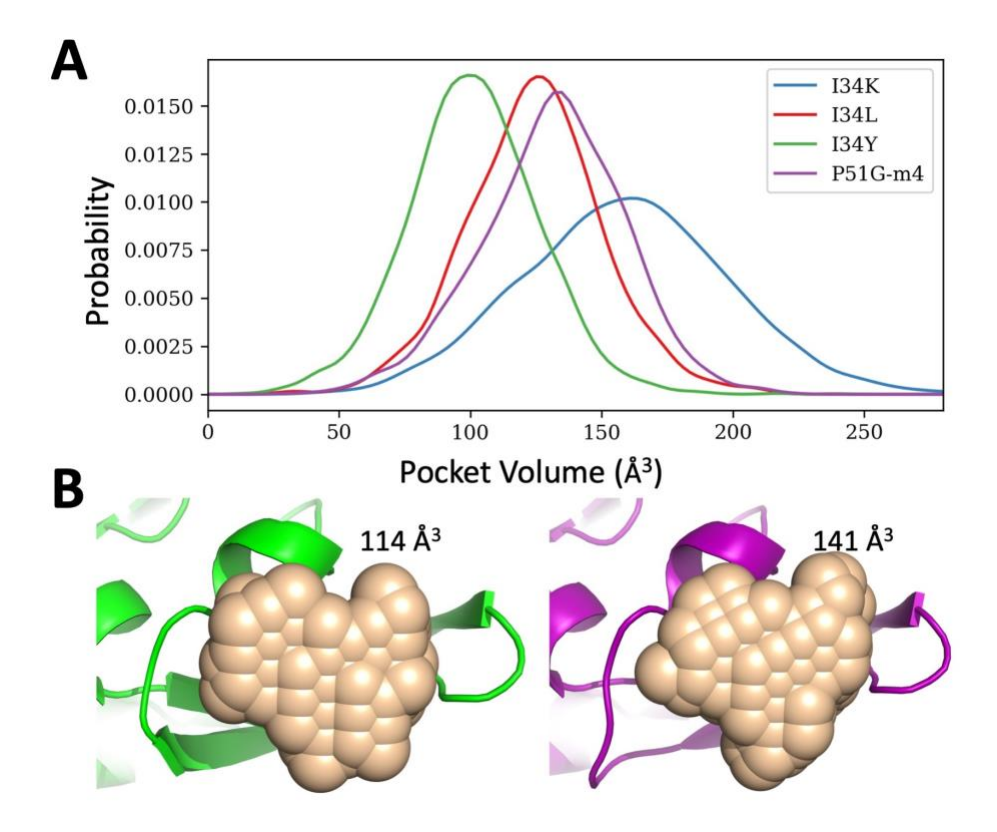


Fig 5 A) Probability distribution of the pocket volume analyses obtained from MD simulation trajectories. I34Y populates a conformation with an optimum volume more than others. P51G-m4 and I34L variant sample similar pocket volumes, but I34K variant has a larger pocket volume compared to others. B) Pocket volume comparison of the domain B of solved structures for P51G-m4 (purple) and I34Y variant (green).

Overall, the conformational dynamics analysis of the unbound conformations indicates a shift of the native ensemble towards a smaller pocket volume upon I34Y mutation. This could explain the decrease in the entropic cost of binding observed in ITC results. We also analyzed the binding energetics by carrying out dimannose docking with 2000 different conformations sampled from the binding pocket volume distributions. We found that the small volume restrict accessibility to the side-chain conformations of binding residue R76 in the I34Y variant, yielding different hydrogen bond patterns with the dimannose (Fig S6) and suggesting a loss in enthalpic contribution.

The bound simulation trajectories were subjected to the MM-PBSA approach to estimate computational binding free energies and related enthalpic and entropic contributions (He et al., 2020; Rastelli et al., 2010). The results are tabulated on Table S4. The computed binding free energies capture the trend of experimental binding affinities (R=0.87). The I34Y variant displays a more favorable binding with dimannose compared to wild type. Interestingly, both experimental and computational results show I34Y compensating the enthalpic loss with entropic gain. While I34L variant enthalpic loss is greater than I34Y in computational approach, the overall binding free energy mirrors the ITC results. Additionally, loss of binding of I34K variant overlaps with the ITC data.

Substitutions of I34 modulates the conformational ensemble leading to change in dimannose binding affinity

369

370

371

372

373

374

375

376

377

378

379

380

381

382

383

384

385

386

367

368

Proteins adapt to a new environment or changes the function of a protein by modulating the native state ensemble through mutations of different positions while keeping the 3-D structure conserved (Campitelli et al., 2020a; Kuriyan and Eisenberg, 2007; Li et al., 2015; Liu and Nussinov, 2017; Modi and Ozkan, 2018; Risso et al., 2018; Tripathi et al., 2015; Woodrum et al., 2013). As, we also observed a similar pattern of conservation of structure yet change in function in our designed CV-N I34 variants, we further analyzed the flexibility profiles of I34 variants. The DFI profiles clustered using principal component analyses (PCA) match the 2-D map of melting temperature and K_d as reaction coordinates, suggesting a correlation between changes in dynamics and changes in function (Fig 6). The 2-D map shows I34L, P51G-m4, and I34Y under the same cluster, with I34L and P51G-m4 close, while I34K is markedly different (Fig 6A). The dendrogram constructed based on the DFI profiles captures this clustering (Fig 6B) with P51G-m4 and I34L variant under the same branch, suggesting their dynamics are very similar; I34Y is under the same main cluster albeit in a different branch. I34K is under a separate branch, indicating different dynamics. This is in agreement with our previous studies, where substitutions on DARC spots modulates binding dynamics reflected in their flexibility profiles to adapt to a new environment (Campitelli et al., 2021, 2020b; Kumar et al., 2015b; Modi et al., 2021a).

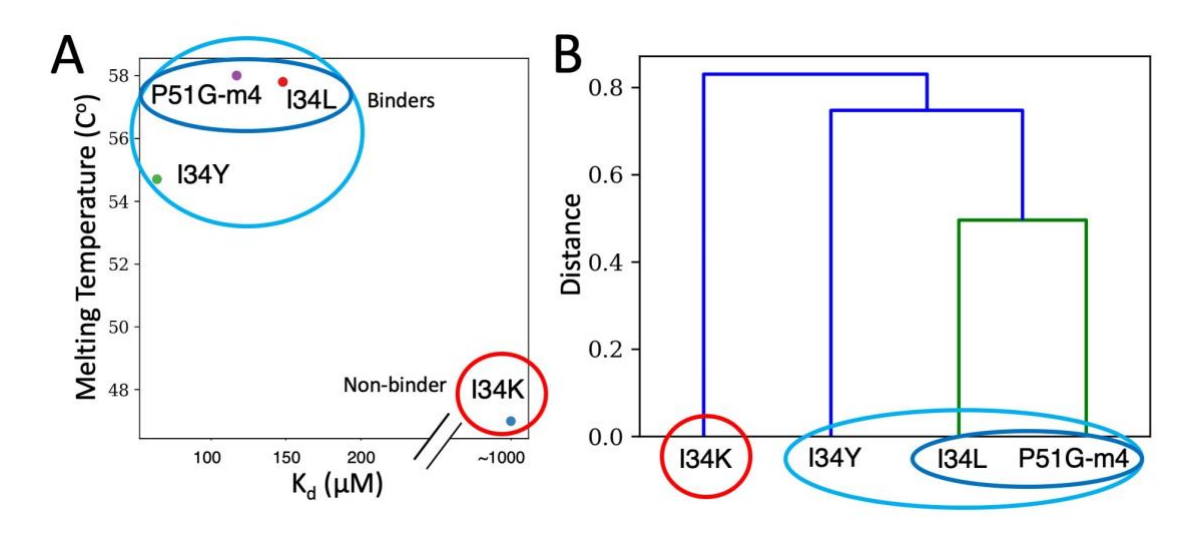


Fig 6 A) 2D map of K_d and Melting temperature of P51G-m4 and its variants B) PCA clustering on the first two principal components of the DFI profiles as a dendrogram.

We further gleaned a molecular view of the role of flexibility in binding by comparing changes in DFI profiles of the binding site residues with P51G-m4 for each mutant, in the unbound and bound form (Fig 7A and B). We found that flexibility at position T57 is highly dependent on the amino acid at position I34: flexibility increases in I34K, suggesting a higher entropic penalty for binding interactions; It is unchanged in I34L, which has similar binding affinity. In contrast, T57 becomes much more rigid in I34Y mutant. This indicates the rigidification leading to a decrease in the entropic cost can contribute to the binding affinity enhancement of this mutant which is also in agreement with the ITC results.

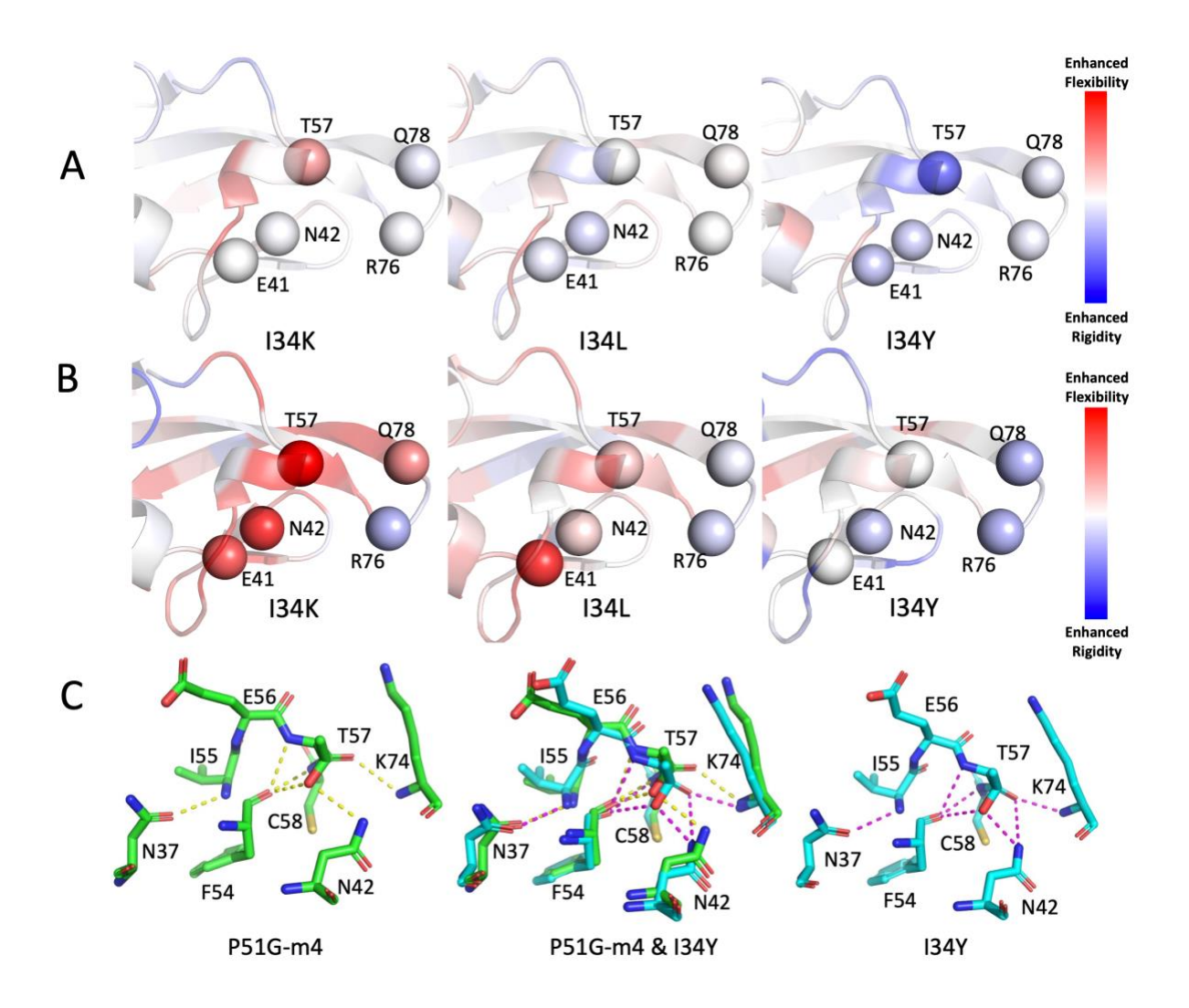


Fig 7 A) Change in flexibility of I34K, I34L, and I34Y relative to P51G-m4 in unbound form are shown. Residues E41, N42, and T57 rigidifies on I34Y compared to P51G-m4. B) Change in flexibility of I34K, I34L, and I34Y relative to P51G-m4 in bound form are projected on structure. C) Hydrogen bonding interactions of residues I55, E56, T57, and C58 are shown for P51G-m4 and I34Y variant.

Comparison of the flexibility profiles of the bound form with those of the unbound form reveals that residue I34 in WT drastically gets rigidified upon binding, whereas I34Y variant does not. The decreased flexibility of T57 in the unbound form of I34Y accommodate the interactions

with dimannose, contributing to the entropic compensation. In addition to the binding site residues of Domain B, the flexibility of the rest of the residues also contribute to the total change in binding free energies. Therefore, we analyzed the correlation between (i) the sum of total change in flexibility of the binding site residues, (ii) the binding site residues and the residues exhibiting highly coupling with the binding pocket, with the experimentally measured binding affinity change. We observe a strong correlation between change in flexibility and change in affinity, as expected I34Y exhibiting tighter binding also gets more rigidified upon binding compared to P51G-m4. Moreover, inclusion of the highly coupled residues in addition to the domain B binding sites in computing the total sum of DFI scores yields a higher correlation with the experimental binding affinity change (Fig S7A). On the other hand, the correlation between the flexibility change of the randomly selected residues and experimental binding affinities yields poor correlation coefficient (Fig S7B). These results strongly support the role of dynamic allostery in modulating binding affinity.

The rigidification of T57 in I34Y variant is compelling evidence that the distal mutation is allosterically controlling the binding site dynamics. We further computed the network of interactions that connects the residue position 34 to 57 and investigated whether distinct pathways emerge after I34Y mutation. We analyzed the hydrogen bond networks, particularly computed the possible network of hydrogen bonds creating pathways from 34 to 57 using the sampled snapshots from the MD trajectories (Fig S8). This analysis presents a unique pathway from 34 to 57 by first forming a new hydrogen bond between the side chain oxygen of the Tyrosine 34 and the nitrogen of the Tyrosine 100 in I34Y variant. Furthermore, a second pathway is also found which is sampled

much more frequently in I34Y variant strengthening the communication between position 34 and 57. Thus, both pathways may contribute to the rigidification of T57. We also analyzed the conformations from MD clustered with highest percentage based on alpha carbon RMSD for I34Y and P51G-m4 and compared the hydrogen bond interactions of T57 and its neighboring residues. The closest neighbors of T57; positions I55, E56, and C58 conserved their hydrogen bond interactions with their surrounding residues between P51G-m4 and I34Y. On the other hand, T57 makes an additional hydrogen bond interaction in I34Y compared to P51G-m4 (Fig 7C), suggesting that enhancement in hydrogen bond networking of T57 in I34Y leads to rigidification of this position in equilibrium dynamics.

To gain more insight on distal dynamic modulation of binding pocket particularly the decrease of binding site flexibility through distal coupling, we computationally and experimentally characterized another residue, A71, belonging to category (1,1) and its mutations: T, S. The docking scores and DFI profiles of A71 variants show high similarity to position I34 ones. The variant A71T is predicted as binding enhancing by our docking scheme displaying a similar binding score as I34Y (A71T predicted binding score: -6.81 XEU), whereas variant A71S is predicted as analogous to I34L variant (A71S predicted binding score: -6.20 XEU). This position is next to residue E72, which is within the hydrogen bond pathway (Pathway 2) (Fig S8) identified previously connecting I34 and binding residue T57. Furthermore, the computed binding free energies by MM-PBSA is found to be correlating with position I34 results. The A71T variant shows a binding free energy near I34Y (A71T ΔG: -13.70 kcal/mol with ΔH: -29.33 kcal/mol and TΔS: -15.63 kcal/mol), and A71S close to I34L (A71S ΔG: -9.98 kcal/mol with ΔH: -29.00 kcal/mol and TΔS: -19.02 kcal/mol). All computational analyses suggested that A71 can modulate

binding affinity through distal dynamic coupling similar to I34, hence we experimentally characterized these two variants.

The experimental binding affinity by ITC correlates with *in silico* predictions. When the change in total DFI score upon binding is compared to change in free energy of binding from ITC experiments (Fig S7), A71T (ΔG: -5.70 kcal/mol with ΔH: -6.00 kcal/mol and TΔS: -0.30) features both a change in total DFI and ΔG closer to I34Y, and A71S (A71S ΔG: -5.10 kcal/mol with ΔH: -9.10 kcal/mol and TΔS: -4.00) shows a score identical to I34L. The entropy of A71T shows a similar change as I34Y experimentally (A71T TΔS: -0.30) indicating that the same compensation mechanism is utilized by another category (1,1) residue. A71S is closer to I34L (A71S TΔS: -4.00). Similar to I34Y, the melting temperature of A71T is lower than P51G-m4 (Fig S1). Results of A71 variants further establishes the potential of ICDC and category (1,1) residues in diversely tuning the binding affinity of Domain B of CV-N through playing enthalpy-entropy compensation of binding process.

Our new integrated coevolution and dynamic coupling (ICDC) approach shows that it is possible to identify and incorporate distal mutations into protein design bringing together evolutionary inferences with long-range dynamic communications within the 3-D network of interactions.

Methods

Adaptive BP-Dock

Adaptive backbone perturbation docking, Adaptive BP-Dock in short, allows us to model the interaction between CV-N and glycans *in silico* (Bolia and Ozkan, 2016). Adaptive BP-dock combines the complex simulation of backbone flexibility of a protein into Rosetta's ligand docking application (Davis and Baker, 2009). The common restriction in docking is the implementation of flexibility of receptor and ligand (Davis et al., 2009; Davis and Baker, 2009; DeLuca et al., 2015; Meiler and Baker, 2006). Rosetta included the flexibility of ligand in their monte-carlo sampling approach but lacking full receptor flexibility. This high order challenge is overcome by utilizing Perturbation Response Scanning (PRS) to compute backbone changes during docking (Atilgan and Atilgan, 2009; Bolia et al., 2014b, 2014a; Ikeguchi et al., 2005). This procedure also allows the modeling of transition from an unbound state to a bound state (Bolia and Ozkan, 2016). The computational cost of sampling is reduced by using a coarse-grained approach employing Elastic Network Model (ENM) leading to an efficient way of computing backbone perturbations, mimicking the ligand interacting with receptor (Atilgan et al., 2001, 2010; Atilgan and Atilgan, 2009).

We employed Adaptive BP-Dock in modeling glycan CV-N interactions starting from an unbound conformation of CV-N. The perturbed pose of the protein is calculated using PRS. The structure is then minimized, and the side chains are added at this step. The glycan is docked to the minimized structure using RosettaLigand algorithm. Rosetta samples bound conformations using

a knowledge based potential function and calculates bound pose energies. The lowest energy docked pose is selected and feed back to perturbation step, and the same procedure is followed iteratively until a convergence is reached. At the end of each iteration the lowest energy docked pose is taken and binding score is calculated using an empirical scoring function X-score. X-score energy units (XEUs) has shown to provide higher correlations with experimental results (Wang et al., 2002). The flow of the algorithm is shown in Fig S9. Adaptive BP-Docks iterative algorithm ensures the sampling does not get trapped in a local minimum and reaches a global minimum. The challenge of unbound/bound modeling is solved using the iterative approach as the conformations are led towards a bound pose with the help of PRS.

Molecular Dynamics (MD)

Gromacs simulations are conducted for P51G-m4 CV-N and all the variants in unbound form, and further for P51G-m4 CV-N, I34 variants I34K, I34L, I34Y, and A71 variants A71S, A7T in bound form. (Abraham et al., 2015; Spoel et al., 2005). For each simulation the all-atom system is parametrized with CHARMM36 force field and explicit water model TIP3P. The solvation box is set to be minimum 16Å from the edge of the protein. The system is neutralized by potassium ions to sustain electroneutrality and minimized with steepest descent for 10000 steps. A short-restrained equilibrium is conducted in the constant number of particles, pressure, and temperature ensemble (NPT) for 5 ns using the Berendsen method at 300K temperature and 1 bar pressure. NPT production trajectories were performed with Nose-Hoover and Parrinello-Rahman temperature and pressure coupling methods for 2µs at 300K and 1 bar. For all cases periodic

boundary conditions and particle-mesh Ewald (PME) with interaction cutoff of 12Å is employed with Gromacs version 2018.1.

Dynamic Flexibility Index (DFI)

DFI is a position specific metric that can measures the resilience of a given position to the force perturbations in a protein. It calculates the fluctuation response of a residue relative to the gross fluctuation response of the protein (Kumar et al., 2015b; Larrimore et al., 2017). DFI calculates residue response due to a perturbation by utilizing covariance matrices.

$$[\Delta \mathbf{R}]_{3Nx1} = [\mathbf{H}]_{3Nx3N}^{-1} [\mathbf{F}]_{3Nx1}$$

$$DFI_{i} = \frac{\sum_{j=1}^{N} |\Delta R^{j}|_{i}}{\sum_{i=1}^{N} \sum_{j=1}^{N} |\Delta R^{j}|_{i}}$$

Residue response, $\Delta \mathbf{R}$, is calculated using Linear Response Theory (LRT) by applying force, \mathbf{F} , in multiple directions to mimic isotropic fluctuations. Hessian matrix, \mathbf{H} , contains second derivatives of potentials. The inverse of Hessian matrix, \mathbf{H}^{-1} , contains residue covariances, and interpreted as a covariance matrix. The covariance matrices can be gathered from MD simulations, and also by using Elastic Network Model (ENM) of a protein. In this study, MD covariance matrices have been utilized to incorporate residue interactions accurately.

Residues with low DFI score (below 0.2) are considered as hinge points. These points are communication hubs in this 3-D interaction network. Due to high coordination number, the residues exhibiting low DFI values are crucial as information gateways. While they do not exhibit high residue fluctuation to the perturbations, they quickly transfer the perturbation information to other parts, thus they are in control of collective motion of the protein. A change in low DFI positions (i.e., a mutation) will lead to a transformation in the communication grid and majority of disease-associated (i.e. function altering mutations) are often observed as hinges (Butler et al., 2015; Gerek et al., 2013; Kumar et al., 2015a). The substitution on these site usually alters catalytic activity or binding interaction (i.e., glycans) by modulating equilibrium dynamics (Campitelli et al., 2020a).

Dynamic Coupling Index (DCI)

Dynamic Coupling Index (DCI) exploits the same framework of DFI (Campitelli et al., 2020a; Larrimore et al., 2017). DCI utilizes the residue response fluctuation upon random force perturbation at a specific residue position to investigate residues that exhibit long-range coupling to each other. In DCI approach, a unit force is applied on functional residues (i.e., binding site residues) one by one and responses of all other residues are calculated.

$$DCI_i = rac{\sum_{j}^{N_{Functional}} |\Delta R^j|_i / N_{Functional}}{\sum_{j=1}^{N} |\Delta R^j|_i / N}$$

With DCI scheme the residues with high response (high DCI score) indicates high long range dynamic coupling. Residues with high DCI values with binding sites play a critical role in intercommunication of a protein with the binding residues. These coupled residues are of utmost importance in how forces propagate through amino acid chain network on a binding event. Some of the coupled residues are far from the binding site but still encompass modulation capabilities over binding pocket.

Informing dynamics from co-evolution

Co-evolutionary data paves the way to assessing 3-D structural contacts by utilizing available sequence information (Hopf et al., 2018; Marks et al., 2012; Morcos et al., 2014). Sequence information is more abundant compared to resolved protein structures. Exploiting the sequence information, primary contacts comparable to realistic structural contacts can be calculated and a contact matrix is formed. The accuracy of these contact maps is proved to be valuable in protein folding studies (Kryshtafovych et al., 2019; Morcos et al., 2011; Wang et al., 2016). Evolutionary coupling (EC) analysis is used to collect information on how much two residues in a protein sequence is in close proximity in 3-D structure. EC scores could be calculated by many different statistical approaches. In this study EC information is gathered by using RaptorX, EVcouplings, and MISTIC webservers (Hopf et al., 2019; Simonetti et al., 2013; Wang et al., 2017). While the limitation of these methods emerges from sequence homolog availability of a protein in multiple sequence alignment (MSA), RaptorX uses a deep neural network leveraging joint family approach, combining multiple ortholog protein families sharing similar function and phylogeny, to infer possible contacts. This method is proven to produce high accuracy

in contact prediction compared to others (Wang et al., 2017). However, for a given MSA containing enough homolog sequences other methods are also strong in predicting spatial contacts. EVcouplings approach uses Direct Information (DI) to calculate co-evolutionary couplings. DI metric is a modified mutual information (MI) score considering consistency between pairwise probabilities and single amino acid frequencies (de Juan et al., 2013; Morcos et al., 2011). Nonetheless, MI, a global approach compared to local DI metric, is accurate in capturing true contacts, while entangling indirect contacts from direct contacts. MISTIC web server has taken advantage of MI to calculate co-evolutionary couplings (Dunn et al., 2008; Gouveia-Oliveira and Pedersen, 2007; Simonetti et al., 2013). In their MI method they introduced a correction term to MI to surpass the low statistics gathered with an MSA containing limited number of sequences. This approach is very useful in cases where certain homologs are rare and MSA of these homologs have multiple gaps in their alignments. All of these methods are employed in this study to achieve high accuracy predictions in finding residue couplings.

Mutant proteins cloning, expression, and purification

The genes for mutants (I34Y, I34K, and I34L) were generated by applying mutagenic primers to P51G-m4-gene sequence and amplifying by PCR. The constructs were subsequently cloned in pET26B vector between NdeI and XhoI sites and transformed in BL21(DE3) for expression and purification. The proteins were expressed from a 10 ml starter culture in LB broth overnight at 37 °C, inoculated into 1 L LB medium. The culture was induced with 1 mM isopropyl thiogalactoside (IPTG) when OD reached 0.6 and grown for another 6-8 hours. Then, the cells were harvested by centrifugation, lysed in 6M Guanidine hydrochloride at pH 8.0, and sonicated

for 10 minutes. The supernatant recovered after centrifugation was used to purify proteins with GE HisTrap HP column (GE Healthcare Bio-Sciences, Piscataway, NJ) and a Bio-Rad EconoPump (Bio-Rad, Richmond, CA) under denaturing conditions. In brief, the proteins were loaded on the column in Gu-HCl buffer, which was buffer exchanged by 8M Urea buffer. The nonspecific proteins were washed out by 4M urea and 20mM imidazole buffer, pH 8.0 and eluted with 2M Urea and 200mM imidazole, pH 8.0 buffer before putting it for overnight dialysis against 10 mM Tris pH 8.0 and 100 mM NaCl buffer. The buffer was changed once during the night. The refolded protein was concentrated and re-purified to isolate the monomeric species by size exclusion chromatography using Sephadex 75 10/300 column on Agilent's Infinity 1260 system. The gel filtered protein was finally used for all the experiments.

CD spectroscopy and T-melts

In CV-N family proteins, thermodynamic parameters like free energy of unfolding, enthalpy and entropy cannot be extracted by thermal denaturation because the transition from folded to unfolded state is non-reversible (Patsalo et al., 2011), therefore melting temperatures are used. Far-UV CD spectra were recorded on a Jasco J-815 spectropolarimeter equipped with a thermostatic cell holder, PTC 424S. Spectra were measured from 250 to 200 nm, using a scanning speed of 50 nm/min and a data pitch of 1.0 nm at 25 °C. Samples concentration was approximately 15 μM in 10 mM Tris, pH 8.0 and 100 mM NaCl. For thermal denaturation experiments, the melting profile was monitored at 202 nm from 25 °C to 90 °C. The data points were plotted and fitted in Origin8.5 software to get apparent Tm.

Isothermal titration calorimetry (ITC)

ITC was performed at the Sanford-Burnham Medical Research Institute Protein Analysis Facility using ITC200 calorimeter from Microcal (Northampton, MA) at 23 °C. 2.0 µl aliquots of solution containing between 3mM and 10 mM Man2 were injected into the cell containing between 0.057, and 0.11 mM protein. 19 of 2.0 µl injections were made. The experiments were performed in 10mM Tris, 100mM NaCl, pH 8.0 buffer. ITC data were analyzed using Origin software provided by Microcal.

Chemical denaturation experiments

Chemical denaturation experiments were done by monitoring the shift in the intrinsic tryptophan fluorescence on Cary Eclipse instrument (Varian). 10 µM of protein samples were incubated with increasing concentrations of Guanidine hydrochloride in the range of 0-6 M in 50 mM Tris pH8.0 buffer for 72 hours at 25 °C. The emission spectra for the same were recorded by keeping the excitation wavelength at 295nm and bandwidth of 1 nm. A ratio of fluorescence at 330 and 360 nm (I_{330/360}) was plotted at respective Gu-HCl concentrations, and the data points were fit to following sigmoidal equation to obtain C_m.

641
$$y = A2 + \frac{A1 - A2}{1 + e^{(x-x_0)/dx}}$$

Where, A1 and A2 are the initial and final 330/360 ratios and x0 is the concentration of Gu-HCl, where y=(A1 + A2)/2, or the point where 50 % of the population is unfolded. It is also denoted as C_m .

The denaturation curve was used to calculate the free energy of the protein in the absence of denaturant (ΔG_{H2O}). Fraction unfolded (f_U) was calculated using the following formula:

$$f_{\rm U} = (y_{\rm F} - y_{\rm obs})/(y_{\rm F} - y_{\rm U})$$

where f_U , is the fraction unfolded, y_F is the value when there is no denaturant, y_{obs} is the value at each position and y_U is the value for unfolded protein. Since $f_{U+}f_F=1$, the equilibrium constant, K, the free energy change can be calculated using

 $K = f_{\rm U}/f_{\rm F}$

$$K = f_U / 1 - f_F$$

$$\Delta G = -RT lnK$$

Where R is the gas constant whose value is 1.987 cal/mol.K and T is the temperature of incubation, which was 298K. The value of ΔG is linear over a limited range of Gu-HCl. The linear fit over that range was extrapolated to obtain ΔG_{H2O} .

Crystallization and structure determination

I34Y was purified as discussed previously and the monomeric gel filtered protein was concentrated to 8mg/ml. We got the crystals in 2M ammonium sulphate and 5 % (v/v) 2-propanol after screening it in Index HT screen from Hampton Research. The protein crystals were reproduced using same condition in hanging drop method. For protein crystals with dimannose, the crystals were incubated in 1.2 fold molar excess of dimannose. Single needle-like crystals were picked up and cryo-preserved in 25 % glycerol before freezing them for data collection at Synchrotron ALS, beamline 8.2.1. Single crystal diffraction was measured at wavelength of 0.999 A with ADSC quantum 315 r detector. The data were evaluated to resolution of 1.25 A. The data

668	acquired was indexed using XDS and scaled by the aimless package from CCP4i program suite.
669	The structural coordinates and phase were determined by molecular replacement using 2RDK PDB
670	code. The structure of I34Y of CV-N is deposited under PDB accession code 6X7H. The structure
671	was further refined in Coot.
672	
673	Acknowledgements
674	S.B.O. acknowledges support from the Gordon and Betty Moore Foundations and National
675	Science Foundation (Award: 1715591 and 1901709). This work was supported in part by NIH
676	award 1R21CA207832-01.
677	
678	Competing interests
679	No competing interests declared.
680	
681	Supplementary Data
682	

Table S1. DFI, DCI, RaptorX, Evcoupling, and MISTIC metrics are used to identify residues in TEM-1 β -lactamase for the four unique categories (Supplementary file 1 table 1).

	Dynamically Coupled to Binding Sites 1										Not Dynamically Coupled to Binding Sites 0									
	Residue	DFI Score	DCI Score	Dista			MISTIC Score	EVCOUPLING Score	Current Amino acid	Available Amino acid	Residue	DFI Score	DCI Score	Dista			MISTIC Score	EVCOUPLING Score	Current Amino acid	Available Amino acid
Coevolved with Binding 1 Sites	44	0.20	0.94	14	19	0.92	0.87	0.32	V	AFILMV	51	0.56	0.35	17	24	0.77	0.77	0.92	L	ACEFGIKLM NPQRSTV
	45	0.10	0.89	15	19	0.93	0.99	0.67	G	AGR	121	0.55	0.63	13	17	0.66	0.91	0.91	E	ADEGHKMN QRSTV
	46	0.05	0.86	15	19	0.90	0.88	0.69	Υ	AFGILMTVY	142	0.35	0.52	13	19	0.83	0.61	0.77	1	ACFHILMNQ RSTVY
	47	0.13	0.85	16	20	0.89	0.84	0.97	ı	ACDEFGHIL MNQRSTVW Y	148	0.30	0.68	11	16	0.94	0.78	0.95	L	ADFILMQTV WY
	122	0.15	0.92	10	14	0.71	0.92	0.86	L	ACFHILMSV	155	0.58	0.51	17	23	0.68	0.91	0.91	М	ACEFGHIKL MNPQRSTV W
	137	0.13	0.93	10	15	0.93	0.95	0.95	L	AEFGIKLMQ RSVY	183	0.04	0.50	14	17	0.84	0.97	0.75	Р	ALPS
	179	0.25	0.85	11	13	0.98	0.97	0.93	D	ADGNR	199	0.61	0.45	17	23	0.74	0.99	0.67	L	ILV
	181	0.19	0.90	12	15	0.92	0.99	0.71	т	ACILSTV	220	0.49	0.67	10	16	0.95	0.96	0.99	L	ACEFGHKLM QRSTVWY
	182	0.10	0.70	15	18	0.66	0.98	0.65	М	ACKMNRSTV	222	0.61	0.56	11	18	0.93	0.99	0.74	R	ACGKLNPQR SV
	187	0.08	0.73	13	17	0.84	0.91	0.99	А	ACEGILMNQ RSTV	223	0.71	0.51	14	20	0.88	0.88	0.64	S	ADEGHKLPQ RSTV
	190	0.19	0.78	12	16	0.95	0.94	0.86	L	AFHILMNST VWY	224	0.69	0.59	16	22	0.83	0.68	0.75	А	ADEGHIKLNE RSTVY
	262	0.01	0.94	10	15	0.96	0.64	0.99	V	ACGILNSTV	225	0.74	0.45	15	22	0.84	0.76	0.99	L	AFIKLMQST VW
	263	0.01	0.90	11	15	0.94	0.80	0.99	ı	ACFGILMST V	227	0.98	0.67	20	27	0.66	0.62	0.89	А	ADEFGHIKL MNPQRSTV
	83	0.74	0.89	16	22	0.16	0.41	0.44	R	ADEGHKLM NQRSTVY	35	0.80	0.81	21	27	0.52	0.09	0.53	D	ADEGHIKLM NPQRSTVW Y
	84	0.77	0.84	17	23	0.33	0.41	0.48	V	ACDEFGHIKL MNQRSTVW Y	52	0.75	0.28	21	27	0.44	0.49	0.50	N	ADEFGHIKM NPQRSTV
Not Coevolved with Binding 0 Sites	93	0.92	0.92	19	24	0.16	0.35	0.51	R	ADEHKLNOR STVY	197	0.71	0.42	21	26	0.33	0.39	0.49	E	ACDEGHKLN PQRSTY
	94	0.90	0.93	19	23	0.16	0.29	0.40	R	ACDEFGHIKL MNPQRSTV W	201	0.79	0.43	20	25	0.33	0.09	0.32	L	ACDEFGHIKL MNPQRSTV Y
											289	0.85	0.72	23	30	0.52	0.10	0.50	н	ACDEFGHIKL MNPQRSTV WY

Table S2. DFI, DCI, RaptorX, Evcoupling, and MISTIC metrics are used to identify residues in CV-N for the ICDC categories (Supplementary file 1 table 2).

	Dynamically Coupled to Binding Sites 1									Not Dynamically Coupled to Binding Sites 0															
	Residue								Dista	ince									Dista	nce					
Coevolved with Binding 1 Sites		DFI Score		Minimum	Average	Score Score	Score			Available Amino acid	Residue	DFI Score	DCI Score	Minimum	Average		Score	Score Score		Available Amino acid					
	34	0.17	0.71	16	22	0.65	0.93	0.71	ı	FIKLMVY	18	0.54	0.51	16	21	0.65	0.98	0.84	L	FILMV					
	61	0.15	0.83	11	15	0.81	0.76	0.86	т	ACFIKLMQST VWY	66	0.95	0.27	21	26	0.27	0.91	0.94	S	ADEFGKLMN PQRST					
	71	0.01	0.93	11	13	0.94	0.92	0.98	А	ACDEGQSTV															
	32	0.02	0.91	23	29	0.44	0.92	0.48	S	ACDHLNSTV	65	0.88	0.49	21	24	0.26	0.7	0.69	G	ADEFGHIKN PQRSTWY					
Not Coevolved with Binding 0 Sites	99	0.35	0.85	18	26	0.53	0.3	0.37	К	ADEFHIKLM NQRSTV	67	0.82	0.29	18	23	0.34	0.79	0.86	S	ADEGHIKLM NPQRSTVY					
											88	0.74	0.55	16	23	0.59	0.72	0.73	D	ADEGHNRST					

Table S3. The predicted binding affinities of domain B and comparison with experimental ITC data for wild type, mutDB, and P51G-m4 benchmarking.

Protein	Predicted Binding Score (X-score energy unit)		ITC dimannose ΔH (kcal/mol)	ITC dimannose TΔS (kcal/mol) (T=298K)	ITC dimannose ΔG (kcal/mol)		
Wild Type	-7.08	16 ± 1	-12.5 ± 0.3	-6.00 ± 0.1	-6.50 ± 0.3		
mutDB	-5.97	No-binding	No-binding	No-binding	No-binding		
P51G-m4	-6.62	117 ± 3	-12.3 ± 0.3	-7.00 ± 0.3	-5.30 ± 0.3		

Table S4. Binding free energies, enthalpy and entropy values for wild type CV-N and its variants calculated with MM-PBSA approach applied on dimannose bound MD simulations.

685

Protein	∆H (kcal/mol)	T∆S (kcal/mol)	∆G (kcal/mol)
P51G-m4	-31.13	-18.34	-12.80
134K	-0.03	-51.07	51.04
I34L	-27.54	-17.97	-9.57
134Y	-29.76	-15.72	-14.05

^{*} The ΔG scores displayed in this table correlates with experimental binding scores with an R value of 0.87.

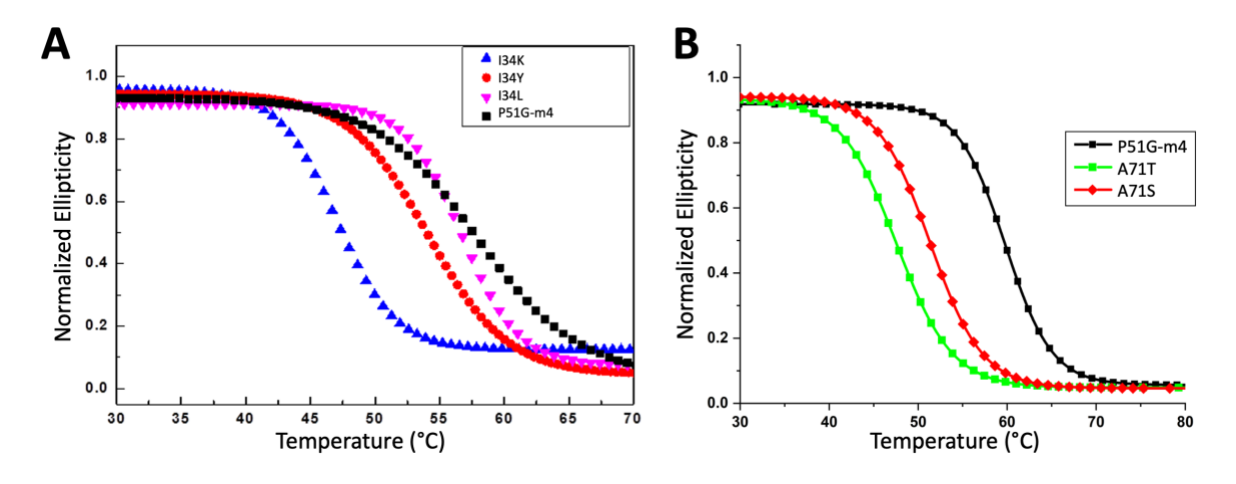


Fig S1 Fits for thermal melts of the CV-N mutants A) I34 variants, and B) A71 variants.

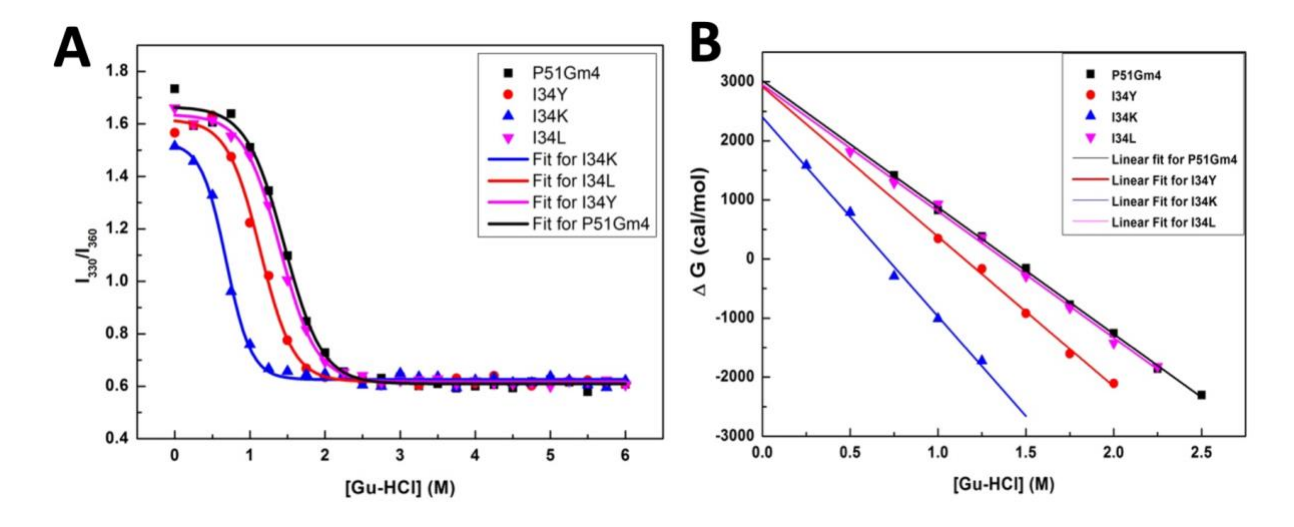


Fig S2 A) Chemical denaturation curve showing I_{330}/I_{360} ratio as a function of Gu-HCl concentration, b) ΔG_{H2O} versus Gu-HCl concentration plot for CV-N mutants.

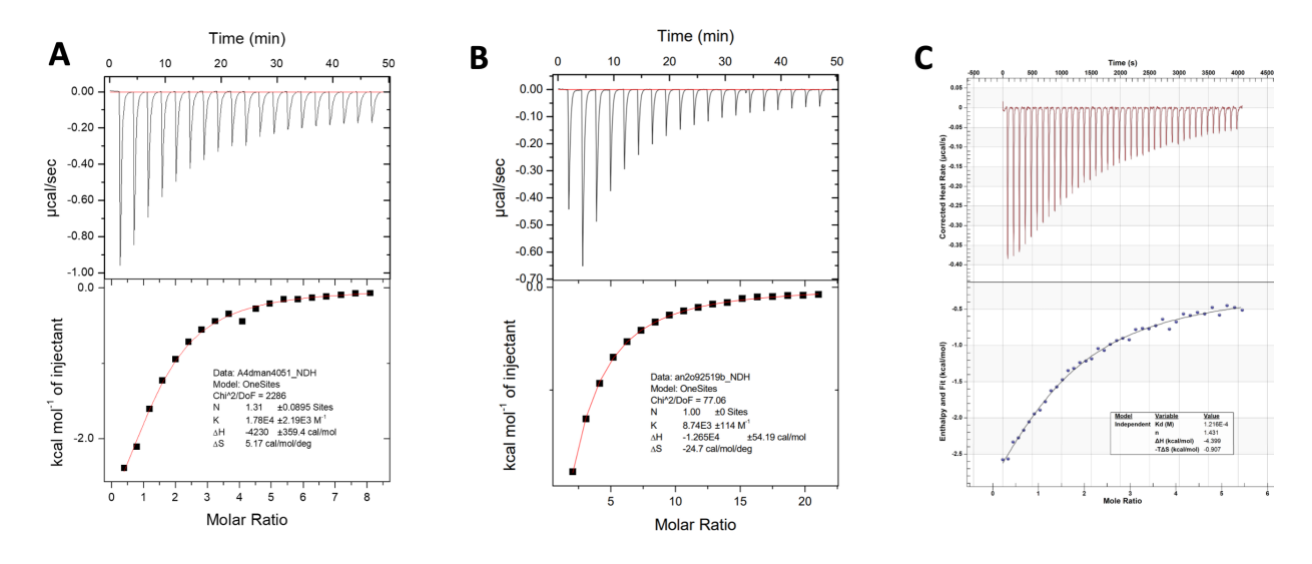


Fig S3 Binding isotherms of CV-N mutants upon titration with dimannose: A) I34Y and B) P51G-m4 C) A71T.

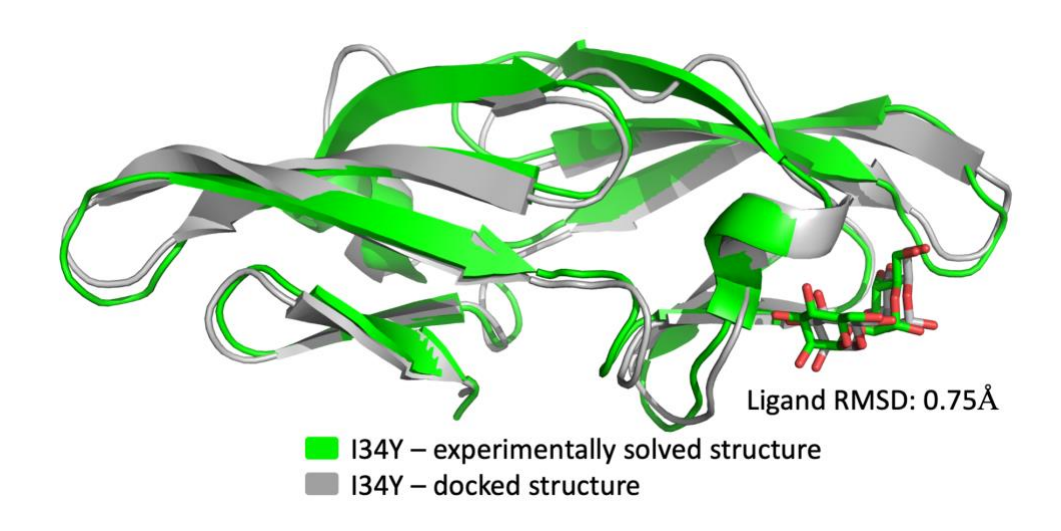


Fig S4 Comparison of experimentally solved I34Y structure with docked pose from Adaptive BP dock algorithm. The RMSD of the ligand is calculated as 0.75 Å.

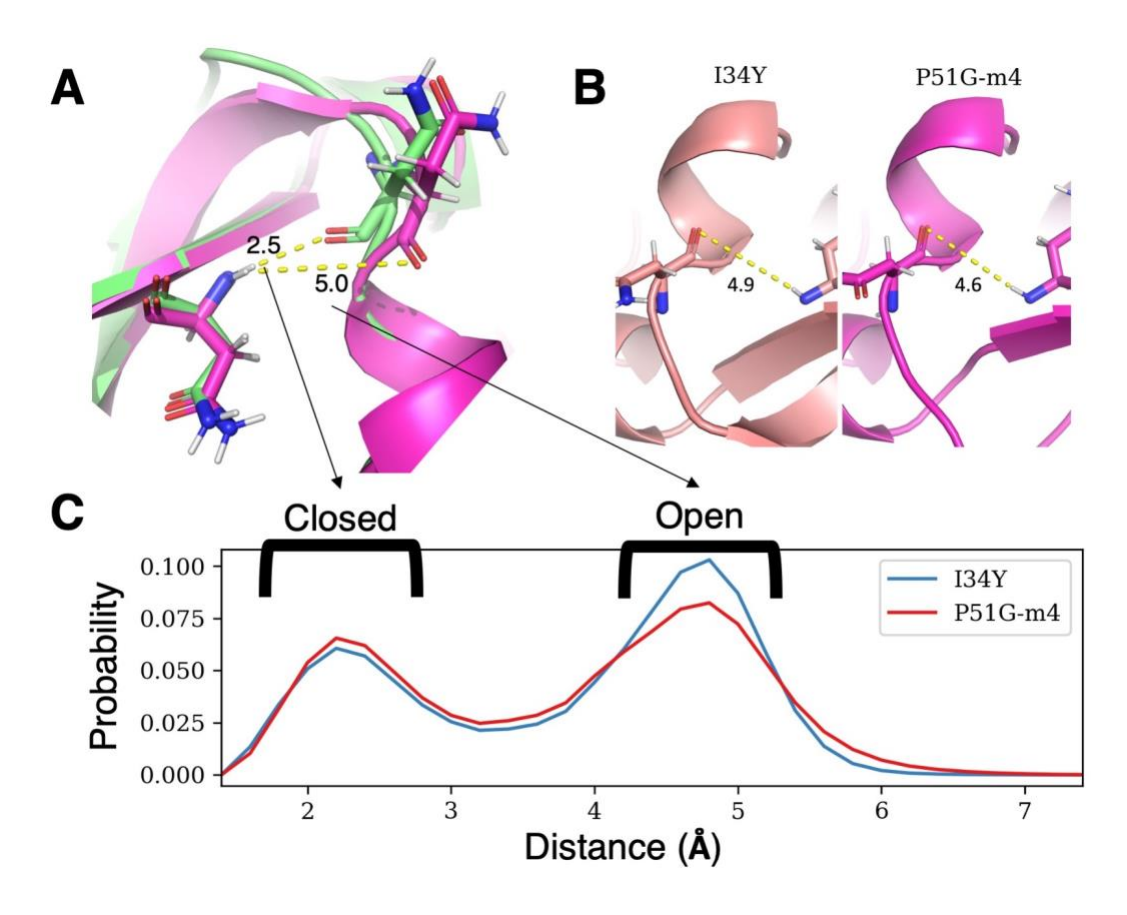


Fig S5 A) Structural difference of open vs closed conformation based on the hydrogen bond distance between residue N42 and N53 B) Hydrogen bond distance between residue N42 and N53 from crystal structures of P51G-m4, and P51G-m4-I34Y C) Frequencies of hydrogen bond distance between residue N42 and N53 from GROMACS production runs showing I34Y variant sampling more open conformation compared to P51G-m4.

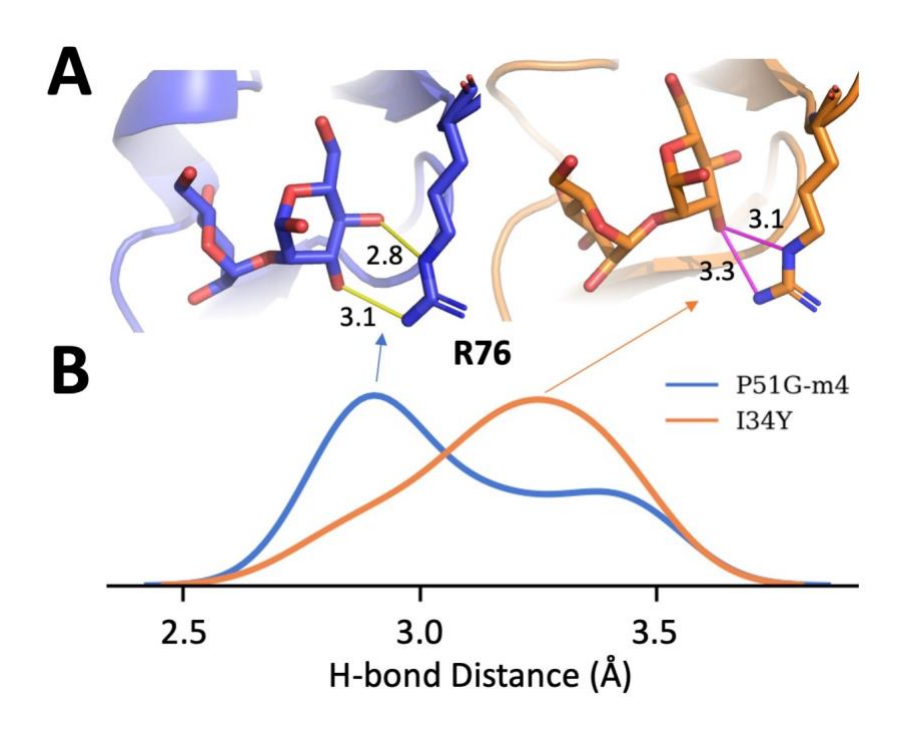


Fig S6 We sampled 2000 different conformations from MD simulations for P51G-m4 CV-N and I34Y mutant and performed dimannose docking to obtained docked poses and then analyzed hydrogen bond patterns A) Hydrogen bonds (representing the peak of the distribution on panel B) and their distances are shown between dimannose and residue R76 for P51G-m4 (blue) and I34Y (orange) B) H-bond distance distribution between dimannose and residue R76.

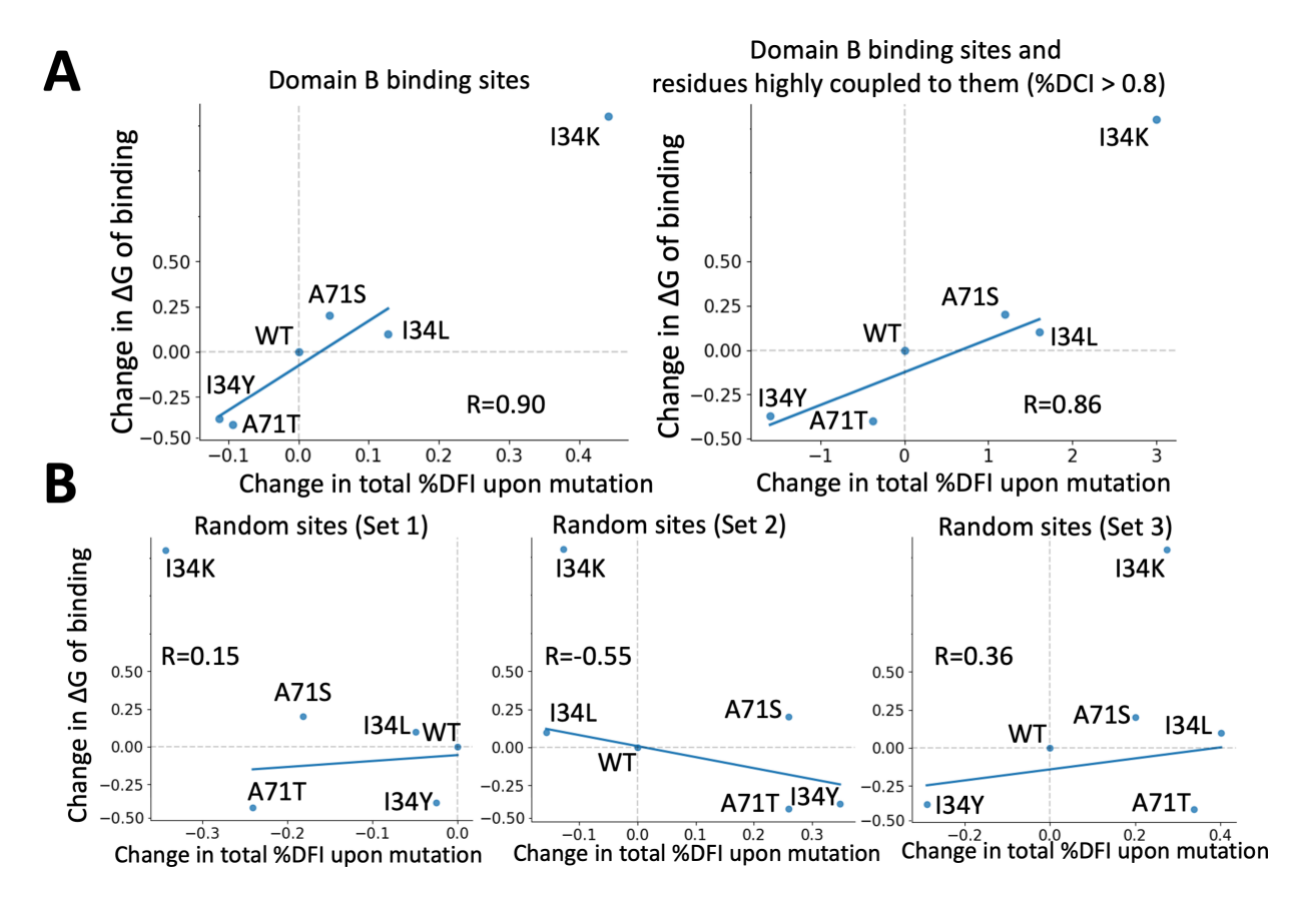


Fig S7 A) Change in ΔG of binding (ΔG_{mut} - ΔG_{wt}) is compared with change in total DFI scores ($\sum DFI_{mut} - DFI_{wt}$) for selected residues. The correlation with experimental binding scores is compared with the total sum of DFI values considering only domain B binding site residues first, and also summing over the domain B binding sites as well as the residues highly coupled (coupling greater than 0.8) to them. The observed high correlations indicates that these residues play an important role in the binding modulation upon mutations. The similar trend has also been seen in LacI (Campitelli et al., 2021) B) In addition we randomly selected residues in domain B to calculate total DFI change over these positions upon mutations. Three different randomly selected residue sets all show poor correlation with change in experimental binding free energy.

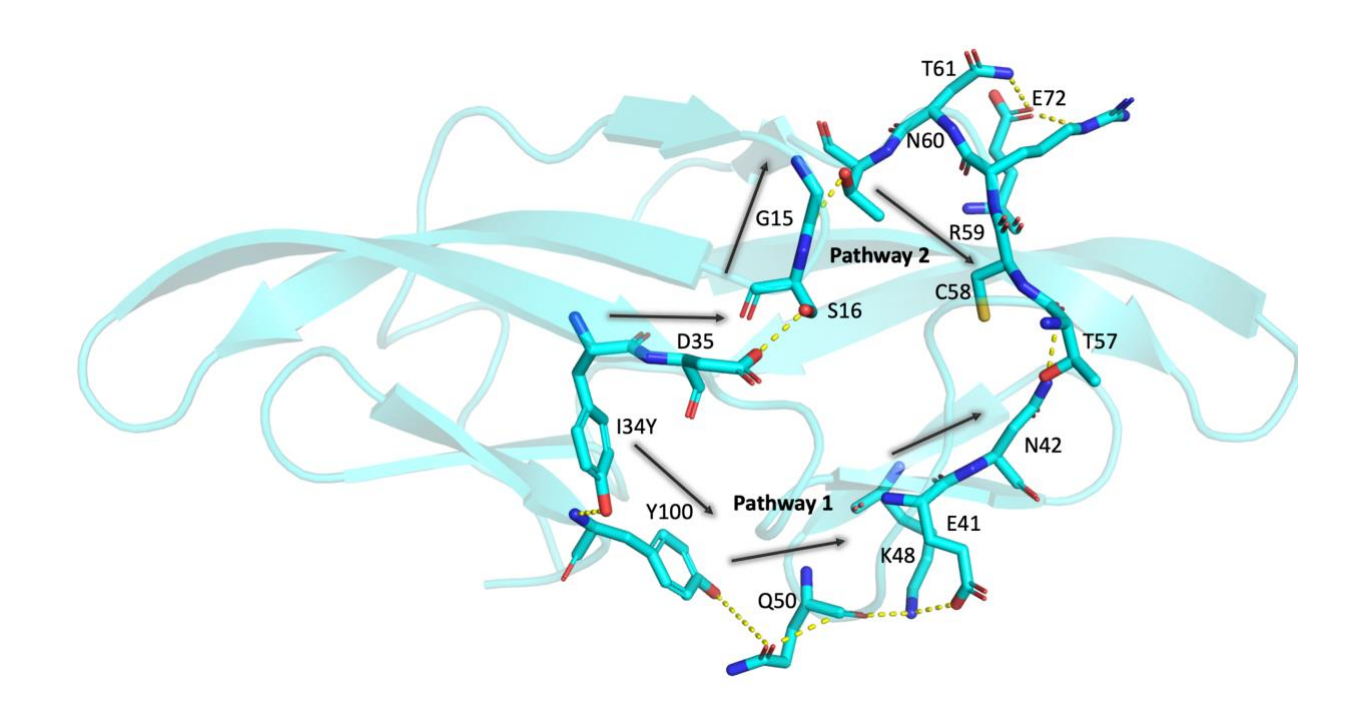


Fig S8 Network of hydrogen bond interactions connecting residue location 34 to T57 is investigated in I34Y variant and P51G-m4 CV-N. Two Hydrogen bond pathways are found connecting residue 34 to 57. Pathway 1 is unique to I34Y. Pathway 2 is also observed in P51G-m4 CV-N but sampled much more frequently in I34Y variant.

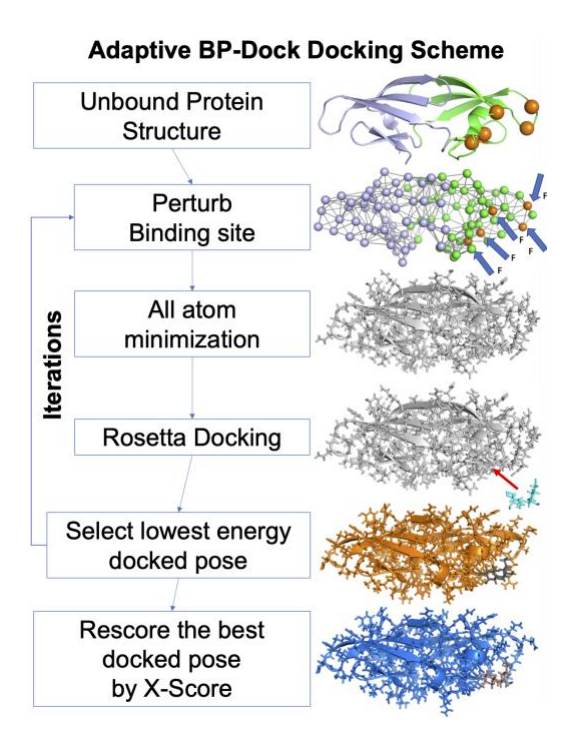


Fig S9 The flow of Adaptive BP-Dock. Starting from an unbound structure the backbone atoms are perturbed using PRS and perturbed pose is fed into minimization. The minimized conformation is docked with the glycan using RosettaLigand docking approach. The lowest scored docked pose is selected and used for next iteration step until convergence is established. For every lowest energy docked pose from an iteration a new binding score is reevaluated using X-score empirical scoring function.

Additional files

Supplementary file 1

This file contains Supplementary Table 1 & 2 (referenced in the main text).

- Supplementary Table 1 contains the complete TEM-1 DFI, DCI, RaptorX, Evcoupling, and
- 707 MISTIC metric data used in this study.
- Note That Supplementary Table 2 contains the complete CV-N DFI, DCI, RaptorX, Evcoupling, and
- 709 MISTIC metric data used in this study.

References

712

722

723

724

725

726 727

728

729

730

731

732

733

734

735

736

737

738

- Abraham MJ, Murtola T, Schulz R, Páll S, Smith JC, Hess B, Lindahl E. 2015. GROMACS:
 High performance molecular simulations through multi-level parallelism from laptops to
 supercomputers. *SoftwareX* **1–2**:19–25. doi:10.1016/j.softx.2015.06.001
- Atilgan AR, Durell SR, Jernigan RL, Demirel MC, Keskin O, Bahar I. 2001. Anisotropy of
 Fluctuation Dynamics of Proteins with an Elastic Network Model. *Biophysical Journal* 80:505–515. doi:10.1016/S0006-3495(01)76033-X
- Atilgan C, Atilgan AR. 2009. Perturbation-Response Scanning Reveals Ligand Entry-Exit
 Mechanisms of Ferric Binding Protein. *PLoS Comput Biol* 5.
 doi:10.1371/journal.pcbi.1000544
 - Atilgan C, Gerek ZN, Ozkan SB, Atilgan AR. 2010. Manipulation of Conformational Change in Proteins by Single-Residue Perturbations. *Biophysical Journal* **99**:933–943. doi:10.1016/j.bpj.2010.05.020
 - Balzarini J. 2007. Targeting the glycans of glycoproteins: a novel paradigm for antiviral therapy. *Nature Reviews Microbiology* **5**:583–597. doi:10.1038/nrmicro1707
 - Barrientos LG, Matei E, Lasala F, Delgado R, Gronenborn AM. 2006. Dissecting carbohydrate—Cyanovirin-N binding by structure-guided mutagenesis: functional implications for viral entry inhibition. *Protein Eng Des Sel* 19:525–535. doi:10.1093/protein/gzl040
 - Barrientos LG, O'Keefe BR, Bray M, Sanchez A, Gronenborn AM, Boyd MR. 2003. Cyanovirin-N binds to the viral surface glycoprotein, GP1,2 and inhibits infectivity of Ebola virus. *Antiviral Research* **58**:47–56. doi:10.1016/S0166-3542(02)00183-3
 - Bewley CA. 2001. Solution Structure of a Cyanovirin-N:Manα1-2Manα Complex: Structural Basis for High-Affinity Carbohydrate-Mediated Binding to gp120. *Structure* **9**:931–940. doi:10.1016/S0969-2126(01)00653-0
 - Bolia A, Gerek ZN, Ozkan SB. 2014a. BP-Dock: A Flexible Docking Scheme for Exploring Protein–Ligand Interactions Based on Unbound Structures. *J Chem Inf Model* **54**:913–925. doi:10.1021/ci4004927
- Bolia A, Ozkan SB. 2016. Adaptive BP-Dock: An Induced Fit Docking Approach for Full
 Receptor Flexibility. *J Chem Inf Model* 56:734–746. doi:10.1021/acs.jcim.5b00587
- Bolia A, Woodrum BW, Cereda A, Ruben MA, Wang X, Ozkan SB, Ghirlanda G. 2014b. A
 Flexible Docking Scheme Efficiently Captures the Energetics of Glycan-Cyanovirin
 Binding. *Biophysical Journal* 106:1142–1151. doi:10.1016/j.bpj.2014.01.040

- Bolmstedt AJ, O'Keefe BR, Shenoy SR, McMahon JB, Boyd MR. 2001. Cyanovirin-N Defines
 a New Class of Antiviral Agent Targeting N-Linked, High-Mannose Glycans in an
 Oligosaccharide-Specific Manner. *Mol Pharmacol* 59:949–954.
 doi:10.1124/mol.59.5.949
- Botos I, Wlodawer A. 2005. Proteins that bind high-mannose sugars of the HIV envelope.
 Progress in Biophysics and Molecular Biology, Structure-guided design of AIDs
 Antivirals 88:233–282. doi:10.1016/j.pbiomolbio.2004.05.001

- Botos I, Wlodawer A. 2003. Cyanovirin-N: a sugar-binding antiviral protein with a new twist. CMLS, Cell Mol Life Sci 60:277–287. doi:10.1007/s000180300023
 - Bowman GR, Geissler PL. 2012. Equilibrium fluctuations of a single folded protein reveal a multitude of potential cryptic allosteric sites. *Proceedings of the National Academy of Sciences* **109**:11681–11686.
 - Breiten B, Lockett MR, Sherman W, Fujita S, Al-Sayah M, Lange H, Bowers CM, Heroux A, Krilov G, Whitesides GM. 2013. Water Networks Contribute to Enthalpy/Entropy Compensation in Protein–Ligand Binding. *J Am Chem Soc* **135**:15579–15584. doi:10.1021/ja4075776
 - Butler BM, Gerek ZN, Kumar S, Ozkan SB. 2015. Conformational dynamics of nonsynonymous variants at protein interfaces reveals disease association. *Proteins: Structure, Function, and Bioinformatics* **83**:428–435. doi:10.1002/prot.24748
 - Campbell E, Kaltenbach M, Correy GJ, Carr PD, Porebski BT, Livingstone EK, Afriat-Jurnou L, Buckle AM, Weik M, Hollfelder F, Tokuriki N, Jackson CJ. 2016. The role of protein dynamics in the evolution of new enzyme function. *Nature Chemical Biology* **12**:944–950. doi:10.1038/nchembio.2175
 - Campitelli P, Guo J, Zhou H-X, Ozkan SB. 2018. Hinge-Shift Mechanism Modulates Allosteric Regulations in Human Pin1. *J Phys Chem B* **122**:5623–5629. doi:10.1021/acs.jpcb.7b11971
 - Campitelli P, Modi T, Kumar S, Ozkan SB. 2020a. The Role of Conformational Dynamics and Allostery in Modulating Protein Evolution. *Annual Review of Biophysics* **49**:267–288. doi:10.1146/annurev-biophys-052118-115517
 - Campitelli P, Ozkan SB, Swint-Kruse L. 2020b. Asymmetry in Dynamic Allosteric Residue Coupling (DARC) Interactions Captures Evolutionary Landscape. *Biophysical Journal* **118**:52a. doi:10.1016/j.bpj.2019.11.464
 - Campitelli P, Swint-Kruse L, Ozkan SB. 2021. Substitutions at Nonconserved Rheostat Positions Modulate Function by Rewiring Long-Range, Dynamic Interactions. *Mol Biol Evol* **38**:201–214. doi:10.1093/molbev/msaa202
 - Chang LC, Bewley CA. 2002. Potent Inhibition of HIV-1 Fusion by Cyanovirin-N Requires Only a Single High Affinity Carbohydrate Binding Site: Characterization of Low Affinity Carbohydrate Binding Site Knockout Mutants. *Journal of Molecular Biology* **318**:1–8. doi:10.1016/S0022-2836(02)00045-1
- Chodera JD, Mobley DL. 2013. Entropy-enthalpy compensation: Role and ramifications in biomolecular ligand recognition and design. *Annu Rev Biophys* **42**:121–142. doi:10.1146/annurev-biophys-083012-130318
- Cornish-Bowden A. 2002. Enthalpy—entropy compensation: a phantom phenomenon. *Journal of Biosciences* **27**:121–126.
- Davis IW, Baker D. 2009. RosettaLigand Docking with Full Ligand and Receptor Flexibility. *Journal of Molecular Biology* **385**:381–392. doi:10.1016/j.jmb.2008.11.010

- Davis IW, Raha K, Head MS, Baker D. 2009. Blind docking of pharmaceutically relevant
 compounds using RosettaLigand. *Protein Science* 18:1998–2002. doi:10.1002/pro.192
- de Juan D, Pazos F, Valencia A. 2013. Emerging methods in protein co-evolution. *Nature Reviews Genetics* 14:249–261. doi:10.1038/nrg3414
 De Luca S, Khar K, Meiler J. 2015. Fully Flexible Docking of Medium Sized Ligand Libra

- DeLuca S, Khar K, Meiler J. 2015. Fully Flexible Docking of Medium Sized Ligand Libraries with RosettaLigand. *PLoS One* **10**. doi:10.1371/journal.pone.0132508
 - Deng Y, Roux B. 2009. Computations of Standard Binding Free Energies with Molecular Dynamics Simulations. *J Phys Chem B* **113**:2234–2246. doi:10.1021/jp807701h
 - Dunn SD, Wahl LM, Gloor GB. 2008. Mutual information without the influence of phylogeny or entropy dramatically improves residue contact prediction. *Bioinformatics* **24**:333–340. doi:10.1093/bioinformatics/btm604
 - Fox JM, Zhao M, Fink MJ, Kang K, Whitesides GM. 2018. The Molecular Origin of Enthalpy/Entropy Compensation in Biomolecular Recognition. *Annual Review of Biophysics* 47:223–250. doi:10.1146/annurev-biophys-070816-033743
 - Fromme R, Katiliene Z, Fromme P, Ghirlanda G. 2008. Conformational gating of dimannose binding to the antiviral protein cyanovirin revealed from the crystal structure at 1.35 Å resolution. *Protein Science* **17**:939–944. doi:10.1110/ps.083472808
 - Fromme R, Katiliene Z, Giomarelli B, Bogani F, Mc Mahon J, Mori T, Fromme P, Ghirlanda G. 2007. A Monovalent Mutant of Cyanovirin-N Provides Insight into the Role of Multiple Interactions with gp120 for Antiviral Activity, *Biochemistry* **46**:9199–9207. doi:10.1021/bi700666m
- Fujimoto YK, Green DF. 2012. Carbohydrate Recognition by the Antiviral Lectin Cyanovirin-N. *J Am Chem Soc* **134**:19639–19651. doi:10.1021/ja305755b
 - Gerek ZN, Kumar S, Ozkan SB. 2013. Structural dynamics flexibility informs function and evolution at a proteome scale. *Evolutionary Applications* **6**:423–433. doi:10.1111/eva.12052
- Gerek ZN, Ozkan SB. 2011. Change in Allosteric Network Affects Binding Affinities of PDZ
 Domains: Analysis through Perturbation Response Scanning. *PLOS Computational Biology* 7:e1002154. doi:10.1371/journal.pcbi.1002154
 - Gouveia-Oliveira R, Pedersen AG. 2007. Finding coevolving amino acid residues using row and column weighting of mutual information and multi-dimensional amino acid representation. *Algorithms for Molecular Biology* **2**:12. doi:10.1186/1748-7188-2-12
 - He X, Liu S, Lee T-S, Ji B, Man VH, York DM, Wang J. 2020. Fast, Accurate, and Reliable Protocols for Routine Calculations of Protein–Ligand Binding Affinities in Drug Design Projects Using AMBER GPU-TI with ff14SB/GAFF. *ACS Omega* 5:4611–4619. doi:10.1021/acsomega.9b04233
 - Hopf TA, Green AG, Schubert B, Mersmann S, Schärfe CPI, Ingraham JB, Toth-Petroczy A, Brock K, Riesselman AJ, Palmedo P, Kang C, Sheridan R, Draizen EJ, Dallago C, Sander C, Marks DS. 2019. The EV couplings Python framework for coevolutionary sequence analysis. *Bioinformatics* **35**:1582–1584. doi:10.1093/bioinformatics/bty862
- Hopf TA, Schärfe CPI, Rodrigues JPGLM, Green AG, Kohlbacher O, Sander C, Bonvin AMJJ,
 Marks DS. 2018. Sequence co-evolution gives 3D contacts and structures of protein
 complexes. *eLife* 3. doi:10.7554/eLife.03430
- Ikeguchi M, Ueno J, Sato M, Kidera A. 2005. Protein Structural Change Upon Ligand Binding: Linear Response Theory. *Phys Rev Lett* **94**:078102. doi:10.1103/PhysRevLett.94.078102

- Jana B, Morcos F, Onuchic JN. 2014. From structure to function: the convergence of structure based models and co-evolutionary information. *Phys Chem Chem Phys* **16**:6496–6507. doi:10.1039/C3CP55275F
- Jiménez-Osés G, Osuna S, Gao X, Sawaya MR, Gilson L, Collier SJ, Huisman GW, Yeates TO, Tang Y, Houk K. 2014. The role of distant mutations and allosteric regulation on LovD active site dynamics. *Nature chemical biology* **10**:431–436.
- Jumper J, Evans R, Pritzel A, Green T, Figurnov M, Ronneberger O, Tunyasuvunakool K, Bates R, Žídek A, Potapenko A, Bridgland A, Meyer C, Kohl SAA, Ballard AJ, Cowie A, Romera-Paredes B, Nikolov S, Jain R, Adler J, Back T, Petersen S, Reiman D, Clancy E, Zielinski M, Steinegger M, Pacholska M, Berghammer T, Bodenstein S, Silver D, Vinyals O, Senior AW, Kavukcuoglu K, Kohli P, Hassabis D. 2021. Highly accurate protein structure prediction with AlphaFold. *Nature* **596**:583–589. doi:10.1038/s41586-021-03819-2

849

850

851

852853

854

855

856

857

858

859

860

861

862

863

864

865866

867

868869

870

871

872

- Kamisetty H, Ovchinnikov S, Baker D. 2013. Assessing the utility of coevolution-based residue—residue contact predictions in a sequence- and structure-rich era. *PNAS* **110**:15674—15679. doi:10.1073/pnas.1314045110
- Kelley BS, Chang LC, Bewley CA. 2002. Engineering an Obligate Domain-Swapped Dimer of Cyanovirin-N with Enhanced Anti-HIV Activity. *J Am Chem Soc* **124**:3210–3211. doi:10.1021/ja025537m
 - Kim DE, DiMaio F, Wang RY-R, Song Y, Baker D. 2014. One contact for every twelve residues allows robust and accurate topology-level protein structure modeling. *Proteins: Structure, Function, and Bioinformatics* **82**:208–218. doi:10.1002/prot.24374
 - Kim H, Zou T, Modi C, Dörner K, Grunkemeyer TJ, Chen L, Fromme R, Matz MV, Ozkan SB, Wachter RM. 2015. A hinge migration mechanism unlocks the evolution of green-to-red photoconversion in GFP-like proteins. *Structure* **23**:34–43.
 - Koharudin LMI, Furey W, Gronenborn AM. 2009. A designed chimeric cyanovirin-N homolog lectin: Structure and molecular basis of sucrose binding. *Proteins: Structure, Function, and Bioinformatics* 77:904–915. doi:10.1002/prot.22514
 - Koharudin LMI, Gronenborn AM. 2013. Sweet entanglements—protein: Glycan interactions in two HIV-inactivating lectin families. *Biopolymers* **99**:196–202. doi:10.1002/bip.22106
 - Koharudin LMI, Viscomi AR, Jee J-G, Ottonello S, Gronenborn AM. 2008. The Evolutionarily Conserved Family of Cyanovirin-N Homologs: Structures and Carbohydrate Specificity. *Structure* **16**:570–584. doi:10.1016/j.str.2008.01.015
 - Kolbaba-Kartchner B, Kazan IC, Mills JH, Ozkan SB. 2021. The Role of Rigid Residues in Modulating TEM-1 β-Lactamase Function and Thermostability. *International Journal of Molecular Sciences* **22**:2895. doi:10.3390/ijms22062895
- Kryshtafovych A, Schwede T, Topf M, Fidelis K, Moult J. 2019. Critical assessment of methods of protein structure prediction (CASP)—Round XIII. *Proteins: Structure, Function, and Bioinformatics* **87**:1011–1020. doi:10.1002/prot.25823
- Kumar A, Butler BM, Kumar S, Ozkan SB. 2015a. Integration of structural dynamics and
 molecular evolution via protein interaction networks: a new era in genomic medicine.
 Current Opinion in Structural Biology, Catalysis and regulation Protein-protein
 interactions 35:135–142. doi:10.1016/j.sbi.2015.11.002
- Kumar A, Glembo TJ, Ozkan SB. 2015b. The Role of Conformational Dynamics and Allostery
 in the Disease Development of Human Ferritin. *Biophysical Journal* 109:1273–1281.
 doi:10.1016/j.bpj.2015.06.060

- 881 Kuriyan J, Eisenberg D. 2007. The origin of protein interactions and allostery in colocalization. 882 Nature 450:983-990. doi:10.1038/nature06524
- 883 Larrimore KE, Kazan IC, Kannan L, Kendle RP, Jamal T, Barcus M, Bolia A, Brimijoin S, Zhan 884 C-G, Ozkan SB. 2017. Plant-expressed cocaine hydrolase variants of 885 butyrylcholinesterase exhibit altered allosteric effects of cholinesterase activity and 886 increased inhibitor sensitivity. Scientific reports 7:10419.
 - Li Z, Bolia A, Maxwell JD, Bobkov AA, Ghirlanda G, Ozkan SB, Margulis CJ. 2015. A Rigid Hinge Region Is Necessary for High-Affinity Binding of Dimannose to Cyanovirin and Associated Constructs. Biochemistry 54:6951–6960. doi:10.1021/acs.biochem.5b00635
 - Liu J, Nussinov R. 2017. Energetic redistribution in allostery to execute protein function. *Proc* Natl Acad Sci U S A 114:7480–7482. doi:10.1073/pnas.1709071114
 - Lu H-M, Liang J. 2009. Perturbation-based Markovian transmission model for probing allosteric dynamics of large macromolecular assembling: a study of GroEL-GroES. PLoS Comput Biol 5:e1000526. doi:10.1371/journal.pcbi.1000526
 - Marks DS, Hopf TA, Sander C. 2012. Protein structure prediction from sequence variation. Nature Biotechnology **30**:1072–1080. doi:10.1038/nbt.2419
 - Matei E, Basu R, Furey W, Shi J, Calnan C, Aiken C, Gronenborn AM. 2016. Structure and Glycan Binding of a New Cyanovirin-N Homolog. J Biol Chem 291:18967–18976. doi:10.1074/jbc.M116.740415
 - Matei E, Furey W, Gronenborn AM. 2008. Solution and Crystal Structures of a Sugar Binding Site Mutant of Cyanovirin-N: No Evidence of Domain Swapping. Structure 16:1183– 1194. doi:10.1016/j.str.2008.05.011
 - Matei E, Louis JM, Jee J, Gronenborn AM. 2011. NMR solution structure of a cyanovirin homolog from wheat head blight fungus. Proteins: Structure, Function, and Bioinformatics **79**:1538–1549. doi:10.1002/prot.22981
 - Meiler J, Baker D. 2006. ROSETTALIGAND: Protein-small molecule docking with full sidechain flexibility. Proteins: Structure, Function, and Bioinformatics 65:538–548. doi:10.1002/prot.21086
 - Meinhardt S, Jr MWM, Parente DJ, Swint-Kruse L. 2013. Rheostats and Toggle Switches for Modulating Protein Function. PLOS ONE 8:e83502. doi:10.1371/journal.pone.0083502
- 911 Miller M, Bromberg Y, Swint-Kruse L. 2017. Computational predictors fail to identify amino 912 acid substitution effects at rheostat positions. Scientific Reports 7:41329. 913 doi:10.1038/srep41329
 - Modi T, Campitelli P, Kazan IC, Ozkan SB. 2021a. Protein folding stability and binding interactions through the lens of evolution: a dynamical perspective. Current Opinion in Structural Biology **66**:207–215. doi:10.1016/j.sbi.2020.11.007
- 917 Modi T, Huihui J, Ghosh K, Ozkan SB. 2018. Ancient thioredoxins evolved to modern-day 918 stability–function requirement by altering native state ensemble. *Philosophical* 919 *Transactions of the Royal Society B: Biological Sciences* **373**:20170184. 920 doi:10.1098/rstb.2017.0184
- 921 Modi T, Ozkan SB. 2018. Mutations Utilize Dynamic Allostery to Confer Resistance in TEM-1 922 β-lactamase. *Int J Mol Sci* **19**. doi:10.3390/ijms19123808
- 923 Modi T, Risso VA, Martinez-Rodriguez S, Gavira JA, Mebrat MD, Van Horn WD, Sanchez-924 Ruiz JM, Banu Ozkan S. 2021b. Hinge-shift mechanism as a protein design principle for 925 the evolution of β -lactamases from substrate promiscuity to specificity. *Nat Commun*

926 12:1852. doi:10.1038/s41467-021-22089-0

887

888

889

890

891

892

893

894

895

896

897

898

899

900

901

902

903

904

905

906

907

908

909

910

914

915

- 927 Morcos F. 2020. Protein conformations à la carte, a step further in de novo protein design. *PNAS* 928 **117**:8674–8676. doi:10.1073/pnas.2004188117
- 929 Morcos F, Jana B, Hwa T, Onuchic JN. 2013. Coevolutionary signals across protein lineages 930 help capture multiple protein conformations. PNAS 110:20533–20538. 931 doi:10.1073/pnas.1315625110
- 932 Morcos F, Pagnani A, Lunt B, Bertolino A, Marks DS, Sander C, Zecchina R, Onuchic JN, Hwa 933 T, Weigt M. 2011. Direct-coupling analysis of residue coevolution captures native 934 contacts across many protein families. PNAS 108:E1293–E1301. 935 doi:10.1073/pnas.1111471108
- 936 Morcos F, Schafer NP, Cheng RR, Onuchic JN, Wolynes PG. 2014. Coevolutionary information, 937 protein folding landscapes, and the thermodynamics of natural selection. PNAS 938 **111**:12408–12413. doi:10.1073/pnas.1413575111
 - Mori T, Boyd MR. 2001. Cyanovirin-N, a Potent Human Immunodeficiency Virus-Inactivating Protein, Blocks both CD4-Dependent and CD4-Independent Binding of Soluble gp120 (sgp120) to Target Cells, Inhibits sCD4-Induced Binding of sgp120 to Cell-Associated CXCR4, and Dissociates Bound sgp120 from Target Cells. Antimicrobial Agents and Chemotherapy 45:664–672. doi:10.1128/AAC.45.3.664-672.2001
 - Okazaki K, Koga N, Takada S, Onuchic JN, Wolynes PG. 2006. Multiple-basin energy landscapes for large-amplitude conformational motions of proteins: Structure-based molecular dynamics simulations. Proceedings of the National Academy of Sciences **103**:11844–11849.
- 948 O'Keefe BR, Smee DF, Turpin JA, Saucedo CJ, Gustafson KR, Mori T, Blakeslee D, Buckheit R, Boyd MR. 2003. Potent Anti-Influenza Activity of Cyanovirin-N and Interactions with 950 Viral Hemagglutinin. Antimicrobial Agents and Chemotherapy 47:2518–2525. doi:10.1128/AAC.47.8.2518-2525.2003
 - Ose N, Butler BM, Kumar A, Ozkan SB, Kumar S. 2020. Dynamic Allosteric Residue Coupling Reveals Disease Mechanism for Gaucher Disease and NSNVS Across the Proteome. Biophysical Journal 118:53a. doi:10.1016/j.bpj.2019.11.472
 - Patsalo V, Raleigh DP, Green DF. 2011. Rational and Computational Design of Stabilized Variants of Cyanovirin-N That Retain Affinity and Specificity for Glycan Ligands. Biochemistry **50**:10698–10712. doi:10.1021/bi201411c
 - Percudani R, Montanini B, Ottonello S. 2005. The anti-HIV cyanovirin-N domain is evolutionarily conserved and occurs as a protein module in eukaryotes. *Proteins*: Structure, Function, and Bioinformatics **60**:670–678. doi:10.1002/prot.20543
 - Qi X, Yang Y, Su Y, Wang T. 2009. Molecular Cloning and Sequence Analysis of Cyanovirin-N Homology Gene in Ceratopteris thalictroides. amfi 99:78–92. doi:10.1640/0002-8444-99.2.78
 - Ramadugu SK, Li Z, Kashyap HK, Margulis CJ. 2014. The Role of Glu41 in the Binding of Dimannose to P51G-m4-CVN. *Biochemistry* **53**:1477–1484. doi:10.1021/bi4014159
- Rastelli G, Rio AD, Degliesposti G, Sgobba M. 2010. Fast and accurate predictions of binding 966 967 free energies using MM-PBSA and MM-GBSA. Journal of Computational Chemistry 968 **31**:797–810. doi:10.1002/jcc.21372
- 969 Risso VA, Sanchez-Ruiz JM, Ozkan SB. 2018. Biotechnological and protein-engineering 970 implications of ancestral protein resurrection. Current Opinion in Structural Biology. 971 Engineering and design: New applications • Membranes **51**:106–115. 972 doi:10.1016/j.sbi.2018.02.007

940

941

942

943

944

945

946

947

949

951

952

953

954

955

956

957

958

959

960

961

962

963

964

- Rivoire O, Reynolds KA, Ranganathan R. 2016. Evolution-Based Functional Decomposition of
 Proteins. *PLOS Computational Biology* 12:e1004817. doi:10.1371/journal.pcbi.1004817
- Romero PA, Arnold FH. 2009. Exploring protein fitness landscapes by directed evolution.
 Nature Reviews Molecular Cell Biology 10:866–876. doi:10.1038/nrm2805

980

981

985

986

987

988

989

990

991

992

993

994

995

996

997

998

999

1000

1001

1002

1006

1007

- 977 Salinas VH, Ranganathan R. 2018. Coevolution-based inference of amino acid interactions 978 underlying protein function. *eLife* 7:e34300. doi:10.7554/eLife.34300
 - Salverda ML, De Visser JAG, Barlow M. 2010. Natural evolution of TEM-1 β-lactamase: experimental reconstruction and clinical relevance. *FEMS microbiology reviews* **34**:1015–1036.
- Schneider SH, Kozuch J, Boxer SG. 2021. The Interplay of Electrostatics and Chemical
 Positioning in the Evolution of Antibiotic Resistance in TEM β-Lactamases. ACS Central
 Science 7:1996–2008.
 - Simonetti FL, Teppa E, Chernomoretz A, Nielsen M, Marino Buslje C. 2013. MISTIC: mutual information server to infer coevolution. *Nucleic Acids Res* **41**:W8–W14. doi:10.1093/nar/gkt427
 - Spoel DVD, Lindahl E, Hess B, Groenhof G, Mark AE, Berendsen HJC. 2005. GROMACS: Fast, flexible, and free. *Journal of Computational Chemistry* **26**:1701–1718. doi:10.1002/jcc.20291
 - Stiffler MA, Hekstra DR, Ranganathan R. 2015. Evolvability as a Function of Purifying Selection in TEM-1 β-Lactamase. *Cell* **160**:882–892. doi:10.1016/j.cell.2015.01.035
 - Swint-Kruse L, Matthews KS, Smith PE, Pettitt BM. 1998. Comparison of simulated and experimentally determined dynamics for a variant of the LacI DNA-binding domain, NLac-P. *Biophysical journal* **74**:413–421.
 - Thomas VL, McReynolds AC, Shoichet BK. 2010. Structural bases for stability–function tradeoffs in antibiotic resistance. *Journal of molecular biology* **396**:47–59.
 - Tokuriki N, Jackson CJ, Afriat-Jurnou L, Wyganowski KT, Tang R, Tawfik DS. 2012. Diminishing returns and tradeoffs constrain the laboratory optimization of an enzyme. *Nature Communications* **3**:1257. doi:10.1038/ncomms2246
 - Torgeson KR, Clarkson MW, Granata D, Lindorff-Larsen K, Page R, Peti W. 2022. Conserved conformational dynamics determine enzyme activity. *Science Advances* **8**:eabo5546.
- Tripathi S, Waxham MN, Cheung MS, Liu Y. 2015. Lessons in Protein Design from Combined Evolution and Conformational Dynamics. *Scientific Reports* **5**:14259. doi:10.1038/srep14259
 - Vorontsov II, Miyashita O. 2009. Solution and Crystal Molecular Dynamics Simulation Study of m4-Cyanovirin-N Mutants Complexed with Di-Mannose. *Biophysical Journal* **97**:2532–2540. doi:10.1016/j.bpj.2009.08.011
- Wagner JR, Sørensen J, Hensley N, Wong C, Zhu C, Perison T, Amaro RE. 2017. POVME 3.0:
 Software for Mapping Binding Pocket Flexibility. *J Chem Theory Comput* 13:4584–4592. doi:10.1021/acs.jctc.7b00500
- Wang R, Lai L, Wang S. 2002. Further development and validation of empirical scoring functions for structure-based binding affinity prediction. *J Comput Aided Mol Des* **16**:11–26. doi:10.1023/A:1016357811882
- Wang S, Li W, Zhang R, Liu S, Xu J. 2016. CoinFold: a web server for protein contact prediction and contact-assisted protein folding. *Nucleic Acids Res* **44**:W361–W366. doi:10.1093/nar/gkw307

Wang S, Sun S, Li Z, Zhang R, Xu J. 2017. Accurate De Novo Prediction of Protein Contact
Map by Ultra-Deep Learning Model. *PLOS Computational Biology* **13**:e1005324.
doi:10.1371/journal.pcbi.1005324

- Wei G, Xi W, Nussinov R, Ma B. 2016. Protein Ensembles: How Does Nature Harness
 Thermodynamic Fluctuations for Life? The Diverse Functional Roles of Conformational
 Ensembles in the Cell. *Chem Rev* **116**:6516–6551. doi:10.1021/acs.chemrev.5b00562
 - Wodak SJ, Paci E, Dokholyan NV, Berezovsky IN, Horovitz A, Li J, Hilser VJ, Bahar I, Karanicolas J, Stock G, Hamm P, Stote RH, Eberhardt J, Chebaro Y, Dejaegere A, Cecchini M, Changeux J-P, Bolhuis PG, Vreede J, Faccioli P, Orioli S, Ravasio R, Yan L, Brito C, Wyart M, Gkeka P, Rivalta I, Palermo G, McCammon JA, Panecka-Hofman J, Wade RC, Di Pizio A, Niv MY, Nussinov R, Tsai C-J, Jang H, Padhorny D, Kozakov D, McLeish T. 2019. Allostery in Its Many Disguises: From Theory to Applications. *Structure* 27:566–578. doi:10.1016/j.str.2019.01.003
 - Woodrum BW, Maxwell JD, Bolia A, Ozkan SB, Ghirlanda G. 2013. The antiviral lectin cyanovirin-N: probing multivalency and glycan recognition through experimental and computational approaches. *Biochem Soc Trans* **41**:1170–1176. doi:10.1042/BST20130154
 - Xu J. 2019. Distance-based protein folding powered by deep learning. *Proceedings of the National Academy of Sciences* **116**:16856–16865. doi:10.1073/pnas.1821309116
 - Yang G, Hong N, Baier F, Jackson CJ, Tokuriki N. 2016. Conformational tinkering drives evolution of a promiscuous activity through indirect mutational effects. *Biochemistry* **55**:4583–4593.
 - Zimmerman MI, Hart KM, Sibbald CA, Frederick TE, Jimah JR, Knoverek CR, Tolia NH, Bowman GR. 2017. Prediction of new stabilizing mutations based on mechanistic insights from Markov state models. *ACS central science* **3**:1311–1321.
 - Zou T, Risso VA, Gavira JA, Sanchez-Ruiz JM, Ozkan SB. 2015. Evolution of Conformational Dynamics Determines the Conversion of a Promiscuous Generalist into a Specialist Enzyme. *Molecular Biology and Evolution* **32**:132–143. doi:10.1093/molbev/msu281
- Zou T, Woodrum BW, Halloran N, Campitelli P, Bobkov AA, Ghirlanda G, Ozkan SB. 2021.
 Local Interactions That Contribute Minimal Frustration Determine Foldability. *J Phys Chem B* 125:2617–2626. doi:10.1021/acs.jpcb.1c00364